High Capacity Semi-Liquid Lithium Sulfur Cells with Enhanced Reversibility for Application in New-Generation Energy Storage Systems

Daniele Di Lecce[a], Vittorio Marangon[a], Almudena Benítez[b], Álvaro Caballero[b], Julián Morales[*,b],

Enrique Rodríguez-Castellón[c] and Jusef Hassoun[*,a,d]

[a]*Department of Chemical and Pharmaceutical Sciences, University of Ferrara, Via Fossato di Mortara, 17, 44121, Ferrara, Italy.*

[b]*Dpto. Química Inorgánica e Ingeniería Química, Instituto de Química Fina y Nanoquímica, Universidad de Córdoba, 14071 Córdoba, Spain.*

[c]*Dpto. de Química Inorgánica, Cristalografía y Mineralogía, Facultad de Ciencias, Universidad de Málaga, 29071 Málaga, Spain.*

[d]*National Interuniversity Consortium of Materials Science and Technology (INSTM) University of Ferrara Research Unit, University of Ferrara, Via Fossato di Mortara, 17, 44121, Ferrara, Italy.*

*Corresponding authors: jusef.hassoun@unife.it; iq1mopaj@uco.es

Keywords

Abstract

Semi-liquid configuration of sulfur cell is proposed as simple strategy to develop high-energy lithium battery. Two solutions of Li_2S_8 in diethylene glycol dimethyl ether (DEGDME), containing either lithium bis(trifluoromethanesulfonyl)imide (LiTFSI) or lithium trifluoromethansulfonate ($LiCF_3SO_3$), are studied as catholytes for Li/S cells exploiting the polysulfides electrochemical reaction at about 2.2 V *vs*. Li^+/Li. X-ray photoelectron spectroscopy (XPS) and thermal analyses, respectively, reveal composition and high-temperature stability of the catholyte solutions. *Ad hoc* study conducted by impedance spectroscopy, voltammetry, and galvanostatic techniques suggests well suitable characteristics in terms of Li^+-transport ability, electrochemical stability window, and

electrode/electrolyte interphase features. Cells with sulfur loading ranging from about 3 to 5 mg cm^{-2} into the solution are successfully studied with remarkable performances in terms of current rates, efficiency and cycle life. Hence, the lithium cells based on the catholyte deliver maximum capacity of the order of 1100 mAh g_S^{-1} at C/10 rate and stable capacity of about 800 mAh g_S^{-1} at C/3 rate with Coulombic efficiency exceeding 99%. Therefore, the catholyte solutions studied herein are considered as a well suitable candidate for high-energy storage in next generation systems, such as the intriguing hybrid and electric vehicles.

Introduction

Nowadays, the lithium-ion battery based on intercalation or insertion electrodes is the most suitable technology for a vast array of widespread essential devices, including laptops, tablets and smartphones, as well as for electric vehicles and stationary storage systems coupled with renewable energy production plants [1,2]. Since it was firstly introduced in the market in early nineties [3], extensive researches over the last three decades have successfully led to a gradual improvement of the lithium-ion technology, which is currently able to ensure a maximum energy density approaching 250 Wh kg^{-1} with high efficiency for thousands of cycles both at laboratory and commercial levels [4–6]. Despite the remarkable performances achieved so far, increasing interest is now devoted towards alternative energy storage systems based on low-cost cathodes reacting with lithium through the multi-electron conversion process, such as the lithium sulfur battery, which has a theoretical energy density with respect to sulfur of about 3600 Wh kg^{-1} (about 2600 Wh kg^{-1} referred to Li$_2$S) [7], thus leading to expected practical energy density values higher than 300 Wh kg^{-1} [8]. Sulfur conversion to Li$_2$S occurs by a multi-step pathway trough polysulfide intermediates, *i.e.*, Li$_2$S$_x$, $2 \leq x \leq 8$, which are soluble in the electrolyte medium for $x \geq 4$ [9]. Hence, dissolved long-chain polysulfides may migrate to the anode side during the electrochemical process and react with the lithium metal, thereby leading to poor Coulombic efficiency, electrode deterioration and cell failure [10,11]. The insulator character of elemental sulfur may further affect the cell

2

performance in terms of cell polarization, rate capability and reversible capacity [12]. Therefore, several strategies have been devoted to overcome these issues [13], including fine engineering of advanced composite electrodes in which sulfur is confined into nanostructured carbon matrixes to effectively mitigate the polysulfide dissolution effects and enhance the cathode conductivity [14]. Carbon nanotubes [15,16], nanospherules [17], nanosheets [18], hierarchical porous carbon [19], three-dimensional graphene [20], as well as other inactive frameworks of various morphologies [21,22], have been reported as suitable sulfur supports. Furthermore, separator modification through carbon meshes, metal organic frameworks and multilayer cathode engineering actually enhanced the cell perfrormances [23–25]. Alkyl carbonates, which are the most used solvents in conventional lithium-ion batteries, can react with polysulfide species and lead to fast cell deterioration, while ether-based compounds, such as 1,3-dioxolane (DOL) and dimethyl ether (DME), have shown remarkable stability in Li-S cell, but high polysulfide dissolution [26]. Gel and polymer electrolytes based on polyethylene oxide have been indicated to mechanically block the polysulfide shuttle process [27], while the addition of $LiNO_3$ to ether-based electrolytes has shown the formation over the lithium-metal of a stable solid electrolyte interphase (SEI) preventing the polysulfide reactions at the anode side [26]. Moreover, solution of glyme with low molecular weight, *i.e.*, $CH_3(OCH_2CH_2)_nOCH_3$ with small n values, dissolving $LiNO_3$ and lithium bis(trifluoromethanesulfonyl)imide (LiTFSI) or lithium trifluoromethansulfonate ($LiCF_3SO_3$) have demonstrated fast Li^+ transport properties, wide electrochemical stability window, suitable SEI-forming properties, as well as both chemical and thermal stability [28]. Despite glymes have slightly higher viscosity than DOL-DME mixtures, particularly by increasing the chain length, they show significantly lower flammability [28,29]. In particular, we demonstrated in recent reports the favorable characteristics of electrolyte solutions based on diethylene glycol dimethyl ether (DEGDME) in terms of both thermal stability and electrochemical properties [15,29]. These solutions may ensure satisfactory lithium ion transport properties, comparable to DOL-DME-based electrolytes, and improved safety, thereby representing an interesting candidate for possible

3

application in Li-S batteries [15,29]. Recently, long-chain polysulfides have been added to the electrolyte solution to efficiently mitigate the cathode dissolution and improve the SEI on lithium [30,31], thus triggering to a viable and simple strategy to develop high-performance Li-S cells, that is, the semi-liquid configuration in which the dissolved polysulfides are employed as the active material [32–40]. Accordingly, we have reported in previous work lithium sulfur batteries coupling C-S composite cathodes with electrolyte formulations based on tetraethylene glycol dimethyl ether (TEGDME) dissolving $LiCF_3SO_3$ and Li_2S_x [30,41]. Furthermore, we have studied a semi-liquid cell which uses a catholyte solution of Li_2S_8, $LiCF_3SO_3$, and $LiNO_3$ in TEGDME reacting on a carbon-coated aluminum foil, thereby demonstrating reversible capacity of about 550 mAh g_S^{-1} and average voltage of 1.8 V [42]. Semiliquid lithium-sulfur batteries represent an important class of high-energy storage systems which merits in our opinion further development in terms of suitable combination of safe solvent and efficient ion conducting lithium salts to improve the cell efficiency, energy density and cycle life.

Herein, we further survey such an intriguing, easy cell configuration by comparing two catholyte solutions formed by combining Li_2S_8, the short-chain DEGDME solvent, either LiTFSI or $LiCF_3SO_3$ salts, and lithium nitrate ($LiNO_3$) film forming additive. Both formulations are expected to benefit from the satisfactory thermal stability and lower viscosity of diglyme with respect to tetraglyme, thus leading to improved electrochemical performances with the aim to match the one of the advanced S-C composite electrodes [15,29]. X-ray photoelectron spectroscopy, thermogravimetric analysis and differential scanning calorimetry measurements are carried out to evaluate composition and thermal behavior of the catholyte. Furthermore, in-depth electrochemical investigation though voltammetry, impedance spectroscopy, and galvanostatic techniques are employed to detect characteristics of the two systems for possible application as alternative, high-performances and low-cost energy storage systems.

Experimental

Diethylene glycol dimethyl ether (DEGDME, anhydrous, 99.5%, Sigma-Aldrich) was dried under molecular sieves (5 Å, Sigma-Aldrich) until the water content was below 10 ppm, as tested through 899 Karl Fischer Coulometer (Metrohm). Two liquid catholytes were prepared by following a procedure developed in our laboratories [30,42]. Elemental sulfur powder (Sigma-Aldrich) and lithium pieces (Rockwood Lithium), respectively in the 4:1 molar ratio, were mixed in DEGDME to get a yellow suspension, which was stirred for 12 h at 80 °C and for two days at room temperature to obtain a dark red catholyte precursor. 1 mol of either lithium bis(trifluoromethanesulfonyl)imide (LiTFSI, Sigma-Aldrich) or lithium trifluoromethansulfonate (LiCF$_3$SO$_3$, Sigma-Aldrich) and 1 mol of lithium nitrate (LiNO$_3$, Sigma-Aldrich) were dissolved into 1 kg of precursor by stirring for 12 h at room temperature. The catholyte solutions, shown in Figure S1 of the Supplementary material and subsequently indicated by the acronyms DEGDME–Li$_2$S$_8$–1m LiNO$_3$–1m LiTFSI and DEGDME–Li$_2$S$_8$–1m LiNO$_3$–1m LiCF$_3$SO$_3$, respectively, had dark red color and nominal Li$_2$S$_8$ content of 5 wt.%. The catholytes preparation was performed inside an Ar-filled glovebox (MBraun, O$_2$ and H$_2$O content below 1 ppm).

Samples for X-ray photoelectron spectroscopy were prepared by depositing few drops of catholyte solution onto Al foil inside a MBraun glovebox (MBraun, O$_2$ and H$_2$O content below 1 ppm), which were transferred to a Buchi glass oven for overnight drying. Then, the samples were collected in Eppendorf vessels, sealed, and moved to the XPS instrument. This operation was carried out through a home-made glovebox with a specific vacuum transference vessel, thus avoiding the contact of the substrates with air. XPS studies were performed through a Physical Electronics spectrometer (PHI Versa Probe II Scanning XPS Microprobe) with monochromatic X-ray Al Kα radiation (100 μm, 100 W, 20 kV, 1,486.6 eV) as the excitation source. High-resolution spectra were recorded at a given takeoff angle of 45° by a concentric hemispherical analyzer operating in the constant pass energy mode at 23.5 eV using a 1400 μm line (with a100 μm

diameter of the X-ray highly focused beam) analysis area. The spectrometer energy scale was calibrated using Cu $2p_{3/2}$, Ag $3d_{5/2}$, and Au $4f_{7/2}$ photoelectron lines at 932.7, 368.2, and 84.0 eV, respectively. Under these conditions, the Au $4f_{7/2}$ line was recorded with 0.73 eV FWHM at a binding energy (BE) of 84.0 eV. A PHI Smart Soft-VP 2.6.3.4 software package was used for acquisition and data analysis. Recorded spectra were always fitted using Gauss−Lorentz curves. Atomic concentration percentages of the characteristic elements of the surfaces were determined taking into account the corresponding area sensitivity factor for the different measured spectral regions.

Coupled thermogravimetric analysis (TGA) and differential scanning calorimetry (DSC) measurements were performed on the DEGDME–Li_2S_8–1m $LiNO_3$–1m LiTFSI and DEGDME–Li_2S_8–1m $LiNO_3$–1m $LiCF_3SO_3$ catholyte solutions through a Metter Toledo-TGA/DSC, by heating the samples at 5 °C min^{-1} in a nitrogen flow.

The ionic conductivity of the catholytes solutions was evaluated by electrochemical impedance spectroscopy (EIS) on symmetrical blocking CR2032 coin-cells (MTI) using stainless steel (SS) current collectors and a Teflon ring spacer to fix the cell constant to 4.0×10^{-2} cm^{-1}. Impedance spectra were recorded through a VersaSTAT MC Princeton Applied Research (PAR, AMETEK) instrument by applying an alternate voltage signal of 10 mV amplitude in the 500 kHz − 1 Hz frequency range.

Carbon electrodes (indicated by C in cell's schemes) were prepared by doctor blade coating of a slurry formed by Super P carbon (90 wt.%, Timcal) and polyvinylidene fluoride (10 wt.%, PVDF 6020, Solef Solvay) in N-methyl pyrrolidone (NMP, Sigma-Aldrich) over a gas diffusion layer foil (GDL ELAT LT1400) [38]. The wet coated foil was dried for about 3 h on a hot plate at 70 °C, cut into the form of either 10 or 14 mm diameter disks, and then dried overnight at 110 °C under vacuum.

CR2032 coin-cells (MTI) were assembled by properly stacking two electrodes (either lithium disks or coated GDL) and one Celgard separator soaked by 80 µl of catholyte solution,

6

corresponding to a sulfur loading of 4.4 and 4.2 mg for DEGDME–Li_2S_8–1m $LiNO_3$–1m LiTFSI and DEGDME–Li_2S_8–1m $LiNO_3$–1m $LiCF_3SO_3$, respectively. Further Li/catholyte/C cells were prepared by using 160 µl of catholyte solution, corresponding to a sulfur loading of 8.9 and 8.4 mg for DEGDME–Li_2S_8–1m $LiNO_3$–1m LiTFSI and DEGDME–Li_2S_8–1m $LiNO_3$–1m $LiCF_3SO_3$, respectively. All the cells were assembled inside an Ar-filled glovebox (MBraun, O_2 and H_2O content below 1 ppm).

The lithium transference numbers (t_{Li}^+) of DEGDME–Li_2S_8–1m $LiNO_3$–1m LiTFSI and DEGDME–Li_2S_8–1m $LiNO_3$–1m $LiCF_3SO_3$ were determined by employing the Bruce-Vincent-Evans method [43]. Chronoamperometry and EIS were performed on symmetrical Li/catholyte/Li T-type cells using several Whatman® GF/D glass fiber separators soaked by the catholyte solution. EIS was carried out before and after chronoamperometry by applying an alternate voltage signal of 10 mV amplitude in the 500 kHz − 100 mHz frequency range. Chronoamperometry was performed by using a voltage of 30 mV for 1.5 h. The lithium transference number was calculated through the equation (1) [43]:

$$t_{Li}^+ = \frac{I_{ss}}{I_0} \frac{\Delta V - I_0 R_0}{\Delta V - I_{ss} R_{ss}} \tag{1}$$

where I_0 and I_{ss} are the initial and steady-state current values of the chronoamperometry measurement, respectively, ΔV is the chronoamperometry voltage, R_0 and R_{SS} are the initial and steady-state interface resistances as determined by EIS.

Lithium stripping-deposition tests were performed on symmetrical Li/catholyte/Li coin-cells at 100 µA cm^{-2} and 1 hour of step time through a MACCOR Series 4000 battery test system. The lithium/catholyte interphase resistance was measured by EIS on symmetrical Li/catholyte/Li coin-cells throughout 30 days, by applying an alternate voltage signal of 10 mV amplitude in the 500 kHz − 100 mHz frequency range through a VersaSTAT MC Princeton Applied Research (PAR, AMETEK) instrument.

7

The electrochemical stability window of the catholyte solutions was determined by linear sweep voltammetry (LSV) and cyclic voltammetry (CV) at a scan rate of 0.1 mV s^{-1} in the anodic and cathodic regions, respectively, on Li/80 µl catholyte/C coin-cells. Fresh cells were cycled at 1 mV s^{-1} within the voltage ranges from 1.8 to 2.8 V, and then used for either LSV or CV. A first cathodic CV scan was performed at 0.1 mV s^{-1} down to 0.01 V, followed by several cycles between 0.01 and 1.2 V. Further CV measurements at 0.1 mV s^{-1} were carried out on Li/80 µl catholyte/C coin-cells within the voltage ranges from 1.8 to 2.8 V and from 2.1 to 2.8 V in order to characterize the electrochemical process of the catholytes. EIS measurements were performed upon the CV measurements by applying an alternate voltage signal of 10 mV amplitude in the 100 kHz – 100 mHz frequency range. The CV, LSV and EIS experiments were carried out through a VersaSTAT MC Princeton Applied Research (PAR, AMETEK) instrument.

Rate capability tests were performed on Li/80 µl catholyte/C coin-cells at current rates of C/10, C/8, C/5, C/3, C/2, 1C and 2C increasing after 10 cycles and then decreasing back to C/10, within the 1.9 – 2.8 V range from C/10 to C/3 and within the 1.7 – 2.8 V range from C/2 to 2C (1C = 1675 mA g$_S^{-1}$). Further rate capability tests have been performed by cycling at C/10, C/8, C/5, C/3, C/2, 1C and 2C rates (1C = 1675 mA g$_S^{-1}$) increasing after 2 cycles and decreasing back to C/10 at the 16th cycle. EIS measurements were performed on the cells at the OCV, after 1 cycle at C/10 (1C = 1675 mA g$_S^{-1}$) and after the rate capability measurement, by applying a voltage signal of 10 mV in the 100 kHz – 100 mHz frequency range. Li/80 µl catholyte/C coin-cells were studied by galvanostatic tests upon 120 cycles at a current rate of C/3 within the 1.8 – 2.8 V range. Further cycling tests at C/20 within the 1.8 – 2.8 V range were performed on Li/160 µl catholyte/C coin-cells. Both specific capacity and specific current values were referred to the nominal sulfur mass in the catholyte solution.

Results and discussion

8

The chemical composition of the two catholyte solutions is investigated by means of X-ray photoelectron spectroscopy (XPS) and reported in Figure 1. The survey spectra of panels a and b reveal similar response for the DEGDME–Li_2S_8–1m $LiNO_3$–1m LiTFSI and DEGDME–Li_2S_8–1m $LiNO_3$–1m $LiCF_3SO_3$ catholytes, respectively, however with different relative intensity of the signals due to the different salts used. Panels c and d of Figure 1, respectively, report the analyses of the S 2p core level spectra of DEGDME–Li_2S_8–1m $LiNO_3$–1m LiTFSI and DEGDME–Li_2S_8–1m $LiNO_3$–1m $LiCF_3SO_3$ catholytes, which represent the most important evidences for the Li_xS_y active material identification. Beside the different relative intensities ascribed to LiTFSI and $LiCF_3SO_3$ salts, the S 2p peaks are fitted by three main doublets S 2$p_{3/2}$ and S 2$p_{1/2}$. The first doublet with main peaks at binding energy (BE) of 167.5 and 168.7 eV in DEGDME–Li_2S_8–1m $LiNO_3$–1m LiTFSI, and 168.7 and 169.9 eV in DEGDME–Li_2S_8–1m $LiNO_3$–1m $LiCF_3SO_3$ are attributed to S bound to O (*i.e.*, $LiN(SO_2CF_3)_2$, $LiCF_3SO_3$, and possibly Li_2SO_3 of the electrolyte salts) [41]. The second doublet at S $p_{3/2}$ binding energy values of 165.4 eV in DEGDME–Li_2S_8–1m $LiNO_3$–1m LiTFSI and 166.1 eV in DEGDME–Li_2S_8–1m $LiNO_3$–1m $LiCF_3SO_3$ are attributed to the Li_2S_8 polysulfide which has nominal concentration in the solution of 5 wt.% [38,44]. However, the presence of minor peaks at BE of 163 and 162 eV does not exclude completely possible presence of small amount of Li_2S_6 and Li_2S_4 into the two catholyte solutions [38,44]. Hence, Figure 1c,d confirm that the active material in the two catholytes is mainly dominated by the Li_2S_8 specie, with possible presence of a minor amount of Li_2S_6 and Li_2S_4. Figures S2a and S3a in Supplementary material show the deconvoluted C 1s core level spectra of both catholytes. These spectra can be decomposed in several contributions, being those at around 284 eV assigned to adventitious carbon and bonds C-C, C-H related to DEGDME. The contribution between 286 and 287 eV is mainly due to the etheric moieties (C-O-C) from DEGDME, presenting a much higher relative intensity in the catholyte with $LiCF_3SO_3$. As expected, a strong contribution at high binding energy (BE > 292 eV) is observed for both catholytes and assigned C-F bonds. Figures S2b and S3b in Supplementary material show the F 1s core level spectra, where two contributions are observed. The main

9

contribution at high binding energy (687.5-688.5 eV) corresponds to CF_n of the fluorinated salts in the catholytes, *i.e.*, LiTFSI, and $LiCF_3SO_3$, respectively, and to polyvinylidene fluoride [45–47]. The low intensity contributions at low binding energy (683-684 eV) can be assigned to impurities of ionic fluorides, probably LiF [48]. Furthermore, Figures S2c and S3c in Supplementary material show the O 1s signal dominated by the component at 532.4 eV is assigned to O bound to S in the solutions ($-SO_3$). The observed contribution at low binding energy in the case of the catholyte with $LiCF_3SO_3$ is due to the oxygen of DEGDME in agreement with that observed in the C 1s spectrum. The N 1s spectra (Figures S2d and S3d) show one contribution around 406-407 eV assigned to the film forming additive (*i.e.*, NO_3^- in $LiNO_3$) [45,46,49]. In the case of the catholyte with LiTFSI, a strong contribution is also observed at about 398 eV due to the imide group [45]. The insets of Figures S2d and S2d in Supplementary material show the Li 1s core level spectra with binding energy values typical of Li^+. The observation of these clear Li 1s signals is relevant if the low sensitivity of this photoemission is considered. For further sample identification, Table S1 in the Supplementary material section reports the atomic composition of the two samples. The more relevant feature is the high concentration of O in the case of the catholyte with $LiCF_3SO_3$. The different XPS response of the two catholyte samples might indicate a different amount of DEGDME adsorbed over the sample holder following the vacuum drying process required to remove the solvent (see the Experimental section for further details about sample preparation for XPS). However, possible significant effect of the sample preparation on the surface composition of the sample may reasonably affect quantitative analysis of the solvent traces. Therefore, our study provides only qualitative information about the chemical species deposited over the sample surface, thereby further confirming the suitability of the already reported Li_2S_8 synthesis herein employed [30,42], while effective quantification of the compound forming the solutions requires *ad hoc* analyses suitable for liquid solutions and able to identify polysulfides with different chain length. In this respect, UV/Vis spectroscopy may recognize long-, mid-, and short-chain lithium polysulfide species in liquid media as well as determine their concentration by using a proper sample
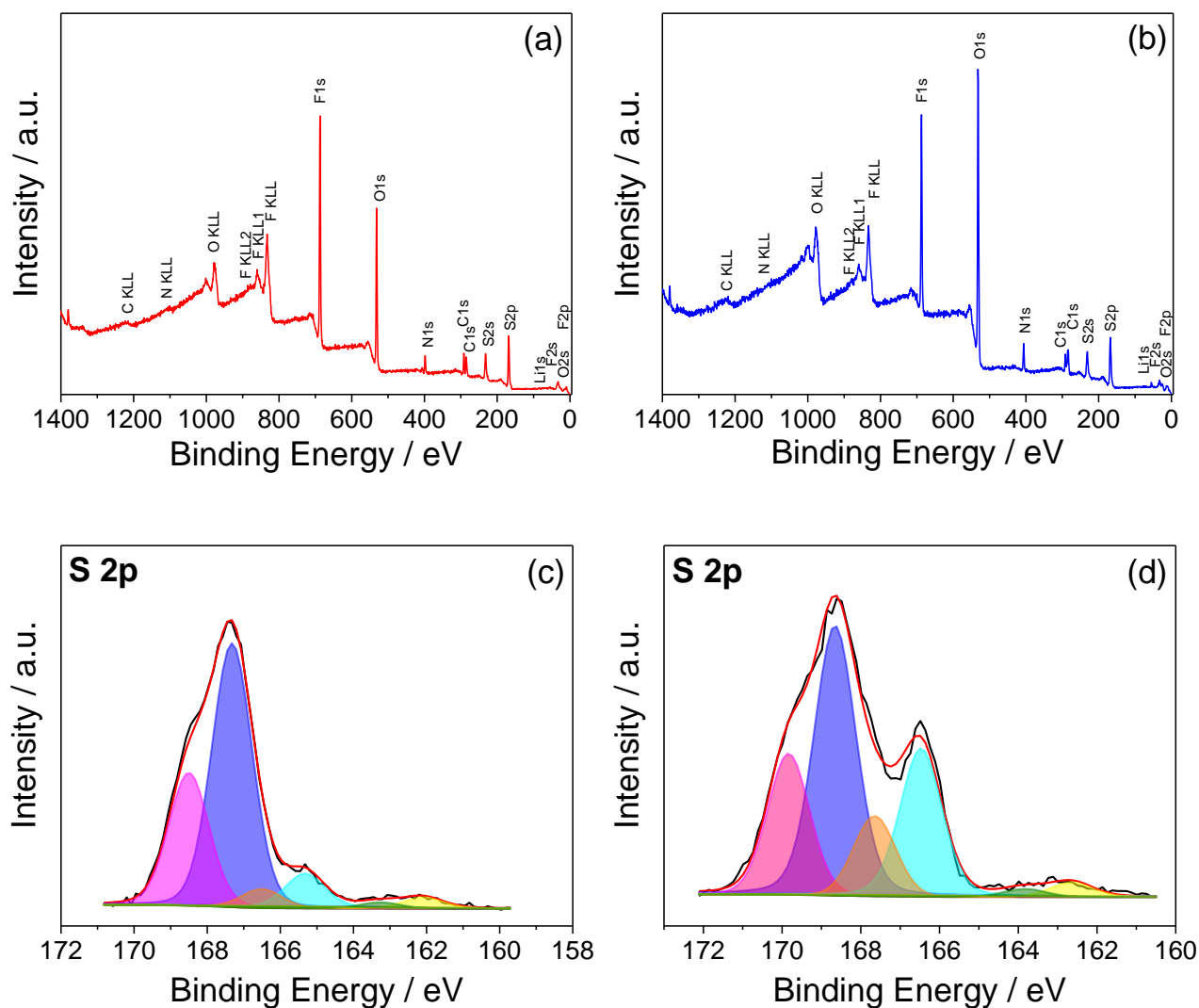
Figure 1. X-ray photoelectron spectra of (**a,c**) DEGDME–Li_2S_8–1m $LiNO_3$–1m LiTFSI and (**b,d**) DEGDME–Li_2S_8–1m $LiNO_3$–1m $LiCF_3SO_3$ catholytes. (**a,b**) Survey spectra and (**c,d**) deconvoluted S 2p core level spectra.

The thermal behavior of the solutions is detected in panels a and b of Figure 2 which show the TGA, differential thermogravimetry (DTG), and DSC traces of the DEGDME–Li_2S_8–1m $LiNO_3$–1m LiTFSI and DEGDME–Li_2S_8–1m $LiNO_3$–1m $LiCF_3SO_3$ catholytes, respectively.
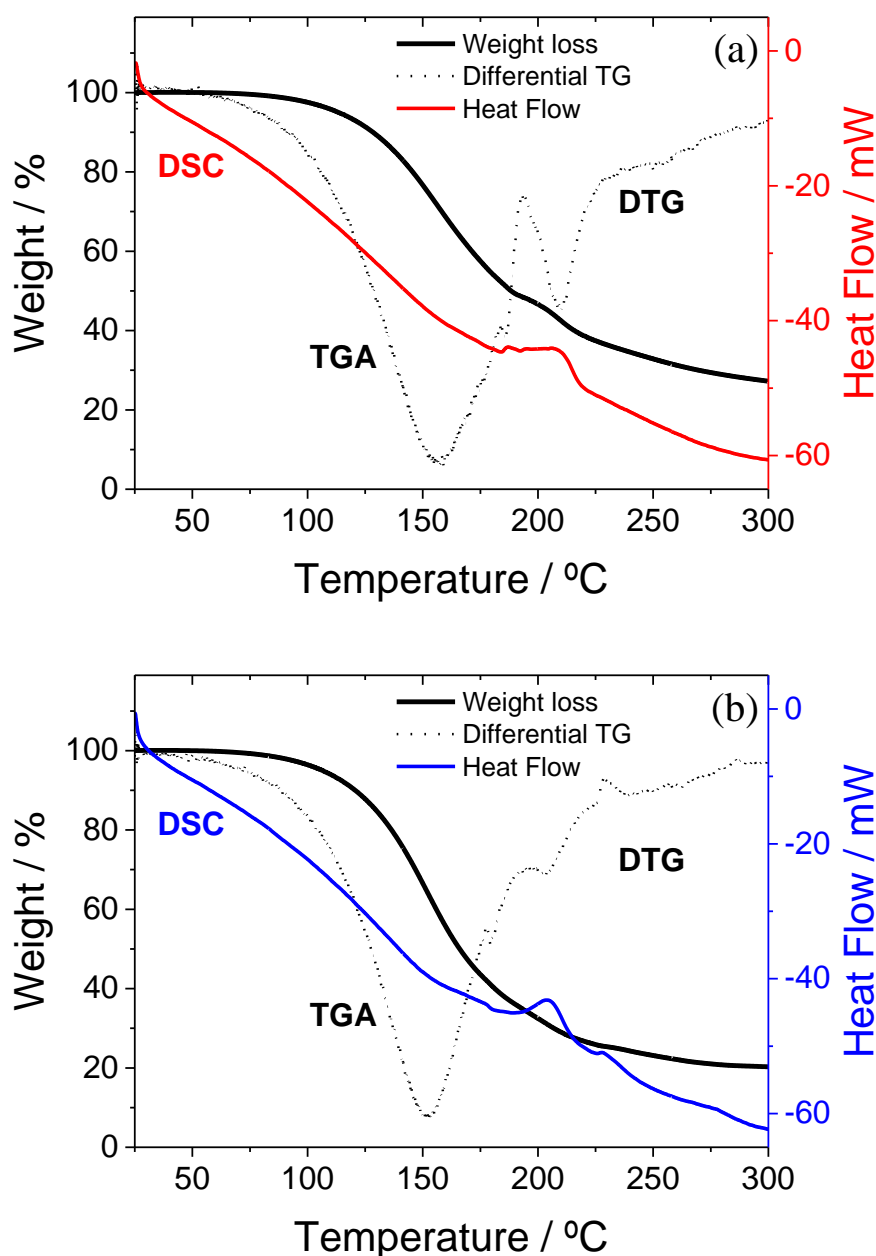
11

Figure 2. Termogravimetric analysis (TGA), corresponding differential curve (DTG), and differential scanning calorimetry (DSC) curves of (**a**) DEGDME–Li$_2$S$_8$–1m LiNO$_3$–1m LiTFSI and (**b**) DEGDME–Li$_2$S$_8$–1m LiNO$_3$–1m LiCF$_3$SO$_3$ samples.

Figure 2a reveals for the DEGDME–Li$_2$S$_8$–1m LiNO$_3$–1m LiTFSI solution a weight loss starting above 70 °C attributed to the initial evaporation of the solution through two main processes, centered at 157 and 210 °C as indicated by TGA and corresponding DTG [28]. The DSC curve (red trace) indicates heat absorption upon the whole investigated temperature range due to evaporation as well as an exothermic peak corresponding to the weight loss at 210 °C observed by TGA/DTG,

which may be reasonably attributed to a solid-state phase transition in LiTFSI (recrystallization) possibly associated with the evaporation of the solvent linked to the salt (*i.e.*, crystallization solvent). The DEGDME–Li_2S_8–1m $LiNO_3$–1m $LiCF_3SO_3$ sample (Figure 2b) exhibits similar thermal behavior upon heating, however with evaporation centered at a slightly lower temperature, *i.e.*, 150 °C, with respect to DEGDME–Li_2S_8–1m $LiNO_3$–1m LiTFSI. Furthermore, a less pronounced DTG peak at 200 °C suggests lower content of the crystallization solvent in $LiCF_3SO_3$ than in LiTFSI (compare panels a and b of Figure 2). Therefore, both catholyte solutions are stable up to about 70-80 °C without showing any significant thermal transition at moderately high temperatures, thereby matching the conventional application requirements [52]. It is worth mentioning that the thermal stability range herein observed is wider than that of common electrolyte solutions both for lithium-ion batteries, based on carbonates-$LiPF_6$ mixtures [53], and for lithium-sulfur batteries, typically containing volatile DOL and DME solvents [28].

The lithium-ion transport properties of the catholyte solutions are crucial parameters for determining the cell performance [15]. Accordingly, fast Li^+ transference within the electrolyte medium can ensure low cell polarization at high current, thus leading to relevant power capability, while hindered mobility usually affects the cell behavior in terms of energy efficiency and rate capability [26]. Herein, we have evaluated the charge transport characteristics of DEGDME–Li_2S_8–1m $LiNO_3$–1m LiTFSI and DEGDME–Li_2S_8–1m $LiNO_3$–1m $LiCF_3SO_3$ by combining ionic conductivity and lithium transference number measurements, as shown in Figure 3a,b and Figure S4 in the Supplementary material, respectively. Both DEGDME–Li_2S_8–1m $LiNO_3$–1m LiTFSI and DEGDME–Li_2S_8–1m $LiNO_3$–1m $LiCF_3SO_3$ catholytes exhibit an Arrhenius trend of the ionic conductivity, reported in panels a and b of Figure 3, with high values within the investigated temperature range [28]. On the other hand, the DEGDME–Li_2S_8–1m $LiNO_3$–1m LiTFSI solution shows slightly higher conductivity than the DEGDME–Li_2S_8–1m $LiNO_3$–1m $LiCF_3SO_3$ one (compare panel a and b of Figure 3), that is, 3×10^{-3} S cm^{-1} with respect to 2×10^{-3} S cm^{-1} at room temperature, increasing to 7×10^{-3} S cm^{-1} with respect to 4×10^{-3} S cm^{-1} by rising the temperature to

about 70 °C. The Arrhenius-like conductivity behavior herein observed is in agreement with previous reports on DEGDME-based solutions for Li-S batteries, and may be reasonably attributed to the low viscosity of short-chain glyme compared with long-chain ones [15,28]. However, it is worth mentioning that deviation from the Arrhenius trend may be expected by cooling below 20 °C as well as by increasing the chain length [54]. The activation energy for the ion transport is 12 and 10 kJ mol^{-1} for DEGDME–Li$_2$S$_8$–1m LiNO$_3$–1m LiTFSI and DEGDME–Li$_2$S$_8$–1m LiNO$_3$–1m LiCF$_3$SO$_3$, respectively, as calculated by conductivity linear trends. Thus, EIS reveals charge transport characteristics approaching those observed in conventional carbonate-based electrolytes for lithium-ion batteries, thereby suggesting the suitability of both solutions for practical applications [55,56]. However, it is noteworthy that the actual charge transference occurring in a lithium cell is only related to the net Li$^+$ flow through the catholyte solution, while the ionic conductivity herein evaluated is attributed to the mobility of all the charge carriers. Therefore, we have determined the Li$^+$ transference number, *i.e.*, the fraction of charge carried by the lithium ion (t$^+$), through the method reported by Evans *et al.* [43] (see the Experimental section for further details). Panel a and b of Figure S4 in Supplementary material section show the related chronoamperometry and EIS Nyquist plots (inset) for DEGDME–Li$_2$S$_8$–1m LiNO$_3$–1m LiTFSI and DEGDME–Li$_2$S$_8$–1m LiNO$_3$–1m LiCF$_3$SO$_3$, respectively. A shift of the left axis intercept is observed after the chronoamperometry measurement (see the Nyquist plots of Figure S4). This evidence reveals an increase of electrolyte resistance, which is possibly attributed to a change of the catholyte composition owing to current flow during the test. Furthermore, electrolyte decomposition over the lithium metal surface during the SEI formation and consolidation, and possible parasitic reactions with partial consumption of the catholyte species may lead to an increase of the cell resistance upon current flow [57]. As for the lithium transference number, both solutions are characterized by high values suitable for lithium cell application, *i.e.*, 0.60 for DEGDME–Li$_2$S$_8$–1m LiNO$_3$–1m LiTFSI and 0.79 for DEGDME–Li$_2$S$_8$–1m LiNO$_3$–1m LiCF$_3$SO$_3$, thereby indicating higher Li$^+$ mobility in the latter than in the former. This result suggests that large fraction of charge

14

upon cell polarization is carried by Li^+ ions, while the mobility of the relatively large NO_3^-, $CF_3SO_3^-$, and $TFSI^-$ is hindered. Furthermore, the latter catholyte is expected to ensure better performance at high current [58].

The stability of the lithium-metal anode in polysulfide-containing electrolytes for Li-S batteries is a key requirement to avoid shuttle reactions, and ensure small cell polarization and long cycle life [59]. Herein, we have investigated the electrochemical characteristics of the lithium/catholyte solution interphase under dynamic and static conditions by performing on Li/Li symmetrical cells lithium plating/stripping tests and EIS measurements during cell aging at room temperature, respectively (Figure 3c-f). Panels c and d of Figure 3 show the voltage profiles for DEGDME–Li_2S_8–1m $LiNO_3$–1m LiTFSI and DEGDME–Li_2S_8–1m $LiNO_3$–1m $LiCF_3SO_3$, respectively, with magnifications in inset revealing the steady-state curves. The former catholyte solution based on the LiTFSI salt exhibits an overvoltage rise during the first day, possibly attributed to gradual formation of a stable solid electrolyte interphase (SEI) on lithium [15], followed by a significant polarization decrease upon the subsequent 15 days indicating partial dissolution and consolidation of the Li^+-conductive passivation layer [60]. Then, the cell shows a constant polarization as low as 7 mV, which suggests remarkable electrochemical stability and low resistance of the SEI upon dynamic condition. As for the latter catholyte based on $LiCF_3SO_3$ salt, Figure 3b reveals a different polarization trend, characterized by an initial voltage approaching 100 mV and a significant polarization decrease down to 10 mV throughout the test owing to the cell operation [15,60]. In particular, the cell shows a steady cycling behavior after 15 days. Therefore, both the DEGDME–Li_2S_8–1m $LiNO_3$–1m LiTFSI and the DEGDME–Li_2S_8–1m $LiNO_3$–1m $LiCF_3SO_3$ catholyte solutions form a remarkably stable SEI over the lithium-metal anode suitable for prolonged Li^+ dissolution and deposition, and able to mitigate the dendrite formation [61]. According to the high lithium transference numbers, both Li/Li cells exhibit flat voltage profile with polarization lower than 10 mV at the steady state, thus suggesting the Li^+ diffusion through the SEI as the limiting step of the electrochemical process at a current of 100 $\mu A\ cm^{-2}$.

15

Figure 3. (**a,b**) Ionic conductivity versus temperature of (**a**) DEGDME–Li$_2$S$_8$–1m LiNO$_3$–1m LiTFSI and (**b**) DEGDME–Li$_2$S$_8$–1m LiNO$_3$–1m LiCF$_3$SO$_3$ catholytes. (**c,d**) Lithium stripping-deposition galvanostatic test performed at 0.1 mA cm^{-2} and 1 hour step-time of (**c**) DEGDME–Li$_2$S$_8$–1m LiNO$_3$–1m LiTFSI and (**d**) DEGDME–Li$_2$S$_8$–1m LiNO$_3$–1m LiCF$_3$SO$_3$ catholytes, with magnifications in panel insets showing steady-state cycles. (**e,f**) Time evolution of the lithium/interface resistance of symmetrical Li/Li cells using (**e**) DEGDME–Li$_2$S$_8$–1m LiNO$_3$–1m LiTFSI and (**f**) DEGDME–Li$_2$S$_8$–1m LiNO$_3$–1m LiCF$_3$SO$_3$ catholytes, and corresponding electrochemical impedance spectroscopy (EIS) Nyquist plots in panel insets. Frequency range: 100 kHz – 100 mHz. Signal amplitude: 10 mV.

16

Panels e and f of Figure 3 report the lithium/catholyte solution interphase resistance trend upon aging of symmetrical Li/Li cells, with the related Nyquist plot in inset, for DEGDME–Li_2S_8–1m $LiNO_3$–1m LiTFSI and DEGDME–Li_2S_8–1m $LiNO_3$–1m $LiCF_3SO_3$, respectively. The Nyquist plots generally reveal an impedance response characterized by high-middle frequency semicircles due to the interphase resistance and a low frequency finite-length Warburg element accounting for Li^+ diffusion phenomena related to non-blocking interphases [62–64]. Figure 3e shows that the Li/DEGDME–Li_2S_8–1m $LiNO_3$–1m LiTFSI resistance varies within the $600 - 900$ Ω range due to recurring SEI dissolution and formation [30], thus reaching a steady state. On the other hand, the Li/DEGDME–Li_2S_8–1m $LiNO_3$–1m $LiCF_3SO_3$ interphase has a resistance of about 800 Ω after 1 day of aging, which increases to about 1200 Ω after 3 days and to about 1600 Ω after 8 days (Figure 3f). Subsequently, the interphase resistance fluctuates between 1400 and 1600 Ω, in agreement with the periodic SEI dissolution and formation as observed also for the DEGDME–Li_2S_8–1m $LiNO_3$–1m LiTFSI solution (compare panels f and e of Figure 3) [30].

Voltammetry and EIS measurements have been carried to investigate the electrochemical stability window of the solutions, the redox processes occurring in lithium cell as well as the cell impedance evolution upon cycling (Figure 4). The voltage stability window has been determined by LSV and CV experiments on Li/catholyte/C cells in the anodic and cathodic regions, respectively. The LSV of DEGDME–Li_2S_8–1m $LiNO_3$–1m LiTFSI (dashed curve in Figure 4a), shows two anodic peaks at 2.4 and 2.5 V related to the reversible catholyte oxidation [9], and the electrolyte decomposition starting at about 4.2 V [28]. The first cathodic CV scan (solid curve in Figure 4 a) reveals the catholyte reduction at about 1.9 and 1.8 V [9], as well as the cathodic electrolyte decomposition at about 1.2 V leading to the SEI formation over the electrodes, while the subsequent cycles within 0.01 and 1.2 V are characterized by overlapped curves indicating steady and reversible Li^+ insertion into the carbon working electrode [15]. The DEGDME–Li_2S_8–1m–$LiNO_3$1m $LiCF_3SO_3$ solution exhibits a similar voltammetry response, as shown in Figure 4b. Thus, the anodic LSV (dashed curve in Figure 4b) indicates decompositions reactions starting at about 4.2

17

V, besides reversible catholyte oxidation at 2.4 and 2.5 V, while the CV (solid curve in Figure 4b) reveals catholyte reduction at 1.9 and 1.6 V [9], SEI formation at 1.2 V, and reversible Li^+ insertion into the carbon working electrode between 0.01 and 1.2 V [15]. Therefore, both the DEGDME–Li_2S_8–1m $LiNO_3$–1m LiTFSI and the DEGDME–Li_2S_8–1m $LiNO_3$–1m $LiCF_3SO_3$ catholyte solutions have an electrochemical stability window from 1.2 to 4.2 V. However, the formation of a stable SEI below 1.2 V leads to a practical voltage window extended down to 0 V, considered suitable for the semi-liquid Li-S cell operation at about 2 V. Panels c and d of Figure 4 show the CV curves within 1.8 and 2.8 V for the two solutions. Figure 4c reveals reversible electrochemical processes which are stable upon cycling, as suggested by overlapping profiles typical of the Li-S conversion reaction [29]. In particular, DEGDME–Li_2S_8–1m $LiNO_3$–1m LiTFSI exhibits two reduction peaks at about 2.4 and 2 V corresponding to the long-chain (Li_2S_6, Li_2S_8) and the short-chain (Li_2S_x, $2 \leq x \leq 4$) sulfide species, which are reversed into two oxidation peaks at 2.3 and 2.5 V related to the stepwise catholyte conversion with Li deposition at the anode side and concomitant S_8 formation [42,65]. Furthermore, possible formation of insoluble Li_2S upon reduction scan below 2 V cannot be excluded [9]. EIS measurements performed during the CV experiment (Figure 4e) reveal a favorable activation process occurring upon cell operation [66,67], which leads to a remarkable cell impedance decrease. Indeed, the Nyquist plot of Figure 4e indicates an electrode/electrolyte interphase resistance at the open circuit voltage (OCV) of about 30 Ω, as revealed by the width of the high-middle frequency semicircle, and a low-frequency Li^+ diffusion response [62–64]. The interphase resistance drops to values as low as about 3 Ω after 5 and 10 cycles, as displayed by magnification in Figure 4e inset, most likely due to an already observed gradual wetting, as well as to progressive surface modification, of the carbon electrode by the catholyte solution, leading to improved reaction kinetics by cycling [66,67]. DEGDME–Li_2S_8–1m $LiNO_3$–1m $LiCF_3SO_3$ shows a CV reported in Figure 4d revealing the reversible Li-S conversion between 1.8 and 2.8 V mostly occurring through overlapping profiles, except for the 1st and 6th cycles which show a different trend with respect to the other cycles likely due the above mentioned

18

activation phenomena [66,67]. Thus, the long-chain (Li_2S_6, Li_2S_8) and short-chain (Li_2S_x, $2 \leq x \leq 4$) polysulfide formation reactions occur at 2.4 and 1.9 V upon discharge, along with possible Li_2S precipitation at about 1.8 V, while the reversed oxidation leads to CV peaks at 2.4 and 2.5 V [42,65]. This activation process is further shown in Figure 4f, which reports the Nyquist plot of the Li/DEGDME–Li_2S_8–1m LiNO$_3$–1m LiCF$_3$SO$_3$/C cell throughout the CV measurement. Accordingly, the cell has initial electrode/electrolyte interphase resistance of about 100 Ω, decreasing to about 15 Ω after 5 and 10 cycles. Despite the DEGDME–Li_2S_8–1m LiNO$_3$–1m LiCF$_3$SO$_3$ catholyte exhibits higher interphase resistance than the DEGDME–Li_2S_8–1m LiNO$_3$–1m LiTFSI one, the observed values, which are comparable with the literature on high performance Li-S cells [15,29,67], indicate fast electrode kinetics for both solutions.

The results shown in Figure 3 c-f suggest that LiTFSI ensures an enhanced SEI layer over the lithium metal with respect to LiCF$_3$SO$_3$, under both static and dynamic conditions. Accordingly, the Li/Li cells using DEGDME–Li_2S_8–1m LiNO$_3$–1m LiTFSI exhibit lower, more stable SEI resistance (see panels c and d of Figure 3), reflected into a lower polarization upon prolonged cycling (see panels e and f of Figure 3) than the ones using DEGDME–Li_2S_8–1m LiNO$_3$–1m LiCF$_3$SO$_3$. Furthermore, Figure 4e-f indicates larger resistance at the electrode/electrolyte interphase for the Li/catholyte/C cell employing LiCF$_3$SO$_3$ as the electrolyte salt. It is worth noting that the impedance measurements of panel e and f of Figure 4 have been performed on two-electrode cells, thereby comprising the contribution of both the anode and the cathode sides. Based on the above mentioned results for the lithium symmetrical cells, we reasonably expect that the higher SEI resistance at the lithium side due to the presence of LiCF$_3$SO$_3$ may contribute to the larger electrode/electrolyte interphase resistance values in Li/C cell compared to LiTFSI. This speculation is in agreement with previous results demonstrating the significant effect of the anion nature on the evolution and transformation of the SEI over lithium metal in polysulfide-containing electrolytes for lithium-sulfur batteries [68,69]. However, we cannot exclude a further effect on the electrode/electrolyte interphase resistance at the cathode side, since the anion nature might

19

influence the electrolyte decomposition product at high voltage. Furthermore, it is worth mentioning that both Li/catholyte/C cells of Figure 4e-f exhibit after cycling low interphase resistance values with same order of magnitude, which may be slightly affected by cell assembling, electrode morphology, and cycling conditions.

Further CV experiments within the restricted voltage range from 2.1 to 2.8 V have been carried out to evaluate the reversibility of the electrochemical process due to Li_2S_6, Li_2S_8 long chain polysulfides and S_8, occurring in Figure 4c-d through current peaks at about 2.4 and 2.5 V upon discharge and charge, respectively. The related profiles are shown in Figure S5 of the Supplementary material. Both DEGDME–Li_2S_8–1m $LiNO_3$–1m LiTFSI and DEGDME–Li_2S_8–1m $LiNO_3$–1m $LiCF_3SO_3$ exhibit remarkably overlapping profiles upon 9 cycles with reversible reduction and oxidation peaks in agreement with Figure 4c-d, as well as cell polarization as low as 0.1 V. This trend suggests a further advantage of the catholyte solutions herein investigated, *i.e.*, a power reservoir associated with the electrochemical reaction of the long-chain polysulfides at about 2.4 and 2.5 V [38]. Therefore, the cell configurations herein studied might be suitable for application in specific fields requiring this particular characteristic, such as the electric vehicles [38].

In summary, CV and EIS reveal and steady electrochemical Li-S conversion processes centered at about 2.4 and 2 V upon reduction, and at about 2.4 V upon oxidation, which occur through fast charge transfer at C electrode/catholyte solution interphase. Our results indicate highly reversible catholyte operation promoted by a cell activation, which remarkably compare previous data obtained on advanced solid sulfur-carbon composite cathodes [15,66]. Moreover, the cell configuration studied herein does not require any fine engineering of cathode and separator, as previously mentioned. Therefore, we believe that the semiliquid cell might be an advantageous strategy to develop Li-S cell without relevant drawbacks in terms of electrochemical behavior with respect to conventional configuration, although suitable performance has been demonstrated only at research level so far.
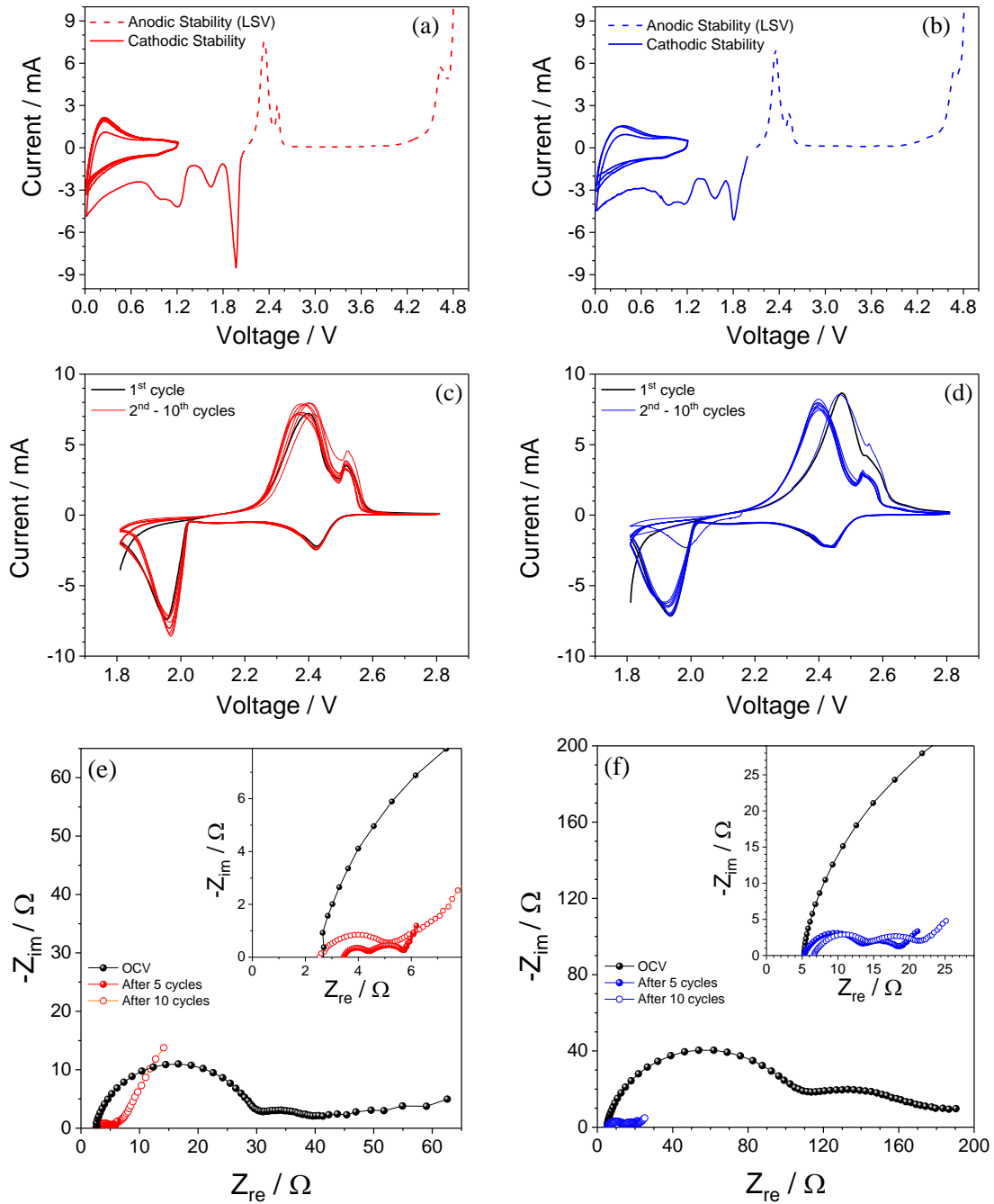
Figure 4. (**a**,**b**) Cyclic voltammetry (CV) profiles during cathodic scans and linear sweep voltammetry (LSV) profiles during anodic scan of lithium cells using carbon working electrode (indicated by C in the cell's schemes) with (**a**) DEGDME–Li_2S_8–1m $LiNO_3$–1m LiTFSI and (**b**) DEGDME–Li_2S_8–1m $LiNO_3$–1m $LiCF_3SO_3$ catholytes. (**c**,**d**) Cyclic voltammetry (CV) profiles of (**c**) Li/DEGDME–Li_2S_8–1m $LiNO_3$–1m LiTFSI/C and (**d**) Li/DEGDME–Li_2S_8–1m $LiNO_3$–1m $LiCF_3SO_3$/C cells within 2.8 V and 1.8 V range. (**e**,**f**) Nyquist plots of the electrochemical impedance spectroscopy (EIS) during CV tests of (**e**) Li/DEGDME–Li_2S_8–1m $LiNO_3$–1m LiTFSI/C and (**f**) Li/DEGDME–Li_2S_8–1m $LiNO_3$–1m $LiCF_3SO_3$/C cells within 1.8 V and 2.8 V range at the OCV, after 5 and 10 cycles with magnification in insets. Scan rate: 0.1 mV s^{-1}. Frequency range: 100 kHz – 100 mHz. Signal amplitude: 10 mV.

21

Nevertheless, an intrinsic gap between fundamental research and practical applications in terms of cell assembling, electrode and electrolyte loading, energy density, performance upon prolonged lithium plating/stripping, and scaling-up may actually raise the issue of large-scale lithium-sulfur cell implementation [7]. Accordingly, further efforts by both academia and industries are certainly required.

The cycling response of the two Li/catholyte/C cells have been herein further evaluated by performing galvanostatic measurements at several current rates. Figure 5 shows the results of a rate capability test of the cells in terms of voltage profiles (panels a, b) and cycling behavior (panels c, d). Both Li/DEGDME–Li_2S_8–1m $LiNO_3$–1m LiTFSI/C and Li/DEGDME–Li_2S_8–1m $LiNO_3$–1m $LiCF_3SO_3$/C cells show the typical voltage curves centered at about 2.2 V, associated with the reversible Li-S conversion [9] with the expected increasing polarization as the C-rate raises. It is worth mentioning that the discharge cutoff of the test has been lowered from 1.9 to 1.7 V for the cycles performed at current rates higher than C/3 in order to allow the reduction to short-chain polysulfides by mitigating the effect of increasing polarization. In agreement with CV, the cells exhibit two discharge plateaus at about 2.4 and 2.1 V, reflected upon charge into plateaus at 2.5 and 2.2 V. The Li/DEGDME–Li_2S_8–1m $LiNO_3$–1m $LiCF_3SO_3$/C cell shows higher rate performances than the Li/DEGDME–Li_2S_8–1m $LiNO_3$–1m LiTFSI/C one in terms of both reversible capacity and polarization at high current (compare panels a and c with panels b and d in Figure 5). In particular, the Li/DEGDME–Li_2S_8–1m $LiNO_3$–1m $LiCF_3SO_3$/C cell delivers higher reversible capacity than the Li/DEGDME–Li_2S_8–1m $LiNO_3$–1m LiTFSI/C one in the current range from C/10 to C/5, *i.e.*, 1160, 1125, and 1050 mAh g_S^{-1} for the former and 1050, 1030, and 1000 mAh g_S^{-1} for the latter, while both catholytes ensure reversible capacity of about 900 mAh g_S^{-1} at C/3 and C/2 (1C = 1675 mA g_S^{-1}). Furthermore, the performance of the Li/DEGDME–Li_2S_8–1m $LiNO_3$–1m $LiCF_3SO_3$/C cell exceeds the one of Li/DEGDME–Li_2S_8–1m $LiNO_3$–1m LiTFSI/C cell at current rates as high as 1C and 2C. Thus, the reversible capacity at 1C and 2C decreases to 740 and 300 mAh g_S^{-1} for the Li/DEGDME–Li_2S_8–1m $LiNO_3$–1m $LiCF_3SO_3$/C cell, and to 115 and 80 mAh g_S^{-1} for the

22

Li/DEGDME–Li$_2$S$_8$–1m LiNO$_3$–1m LiTFSI/C one, respectively, while both cells remarkably recover the initial capacity as the current is decreased to C/10 at the 71st cycle. However, EIS of Figure 4e-f suggests minor difference in terms of electrode/electrolyte interphase resistance between the two cell configurations herein studied, as well as fast electrode charge transfer, after an electrochemical activation likely attributed to already observed gradual wetting and progressive surface modification of the carbon electrode by the catholyte solution [66,67]. Despite the initial interphase resistance is significantly lower when using LiTFSI rather than LiCF$_3$SO$_3$, *i.e.* 30 compared to 100 Ω, respectively, both resistances drop to comparable values as low as 3 and 15 Ω after 10 voltammetry cycles (see Figure 4e-f). We reasonably attribute the poor performance above 1C of the Li/DEGDME–Li$_2$S$_8$–1m LiNO$_3$–1m LiTFSI/C cell to high overvoltage of the processes occurring at the second plateau. In particular, this processes are expected at lower voltage than the discharge cutoff herein used. In operando X-ray Absorption Spectroscopy (XAS) measurements on Li-S cells employing ether-based electrolytes revealed that sulfur conversion and formation of polysulfides mostly occur during the high voltage plateau, while the low voltage plateau is typically characterized by the presence of polysulfides, Li$_2$S and low amount of sulfur [70]. In this respect, it is worth noting that we decreased the discharge cutoff of the test from 1.9 to 1.7 V for the cycles performed at current rates higher than C/3 in order to allow sulfur reduction to short-chain polysulfides and Li$_2$S, mitigate the effect of increasing polarization and by avoid at the same time detrimental nitrate reduction [71].

We have performed herein further EIS measurements on cells studied at various c-rates (from C/10 to 2C) in order to further shed light on the different electrochemical response. EIS measurements have been performed during cycling at various current rates ranging from C/10 to 2C, namely at the OCV, after 1 cycle at C/10 (1C = 1675 mA g$_S^{-1}$) and after the cycling measurement (see the Experimental section for further details). The related Nyquist plots, reported in Figure S7 of the Supplementary material, evidence interphase resistance decreasing from about 75 and 62 Ω at the OCV to values as low as 14 and 7 Ω after 1 cycle at C/10, and 6 and 3 Ω at the

end of the cycling measurement for DEGDME–Li_2S_8–1m $LiNO_3$–1m LiTFSI and DEGDME–Li_2S_8–1m $LiNO_3$–1m $LiCF_3SO_3$, respectively. As already mentioned, we cannot exclude possible effects of cell assembling, electrode morphology, and cycling conditions in determining minor changes of the electrode/electrolyte interphase resistance, thereby considering comparable the EIS response of the cells. Both systems show a significant impedance decrease after cycling due to the already described activation process [66,67]. Accordingly, we may attribute the significantly different response at high current, as well as the observed difference in terms of capacity at the various rates, to the lithium transference numbers of the two catholytes (*i.e.*, 0.60 for DEGDME–Li_2S_8–1m $LiNO_3$–1m LiTFSI and 0.79 for DEGDME–1m $LiNO_3$–1m $LiCF_3SO_3$), which significantly affect cell impedance and polarization [28].

The cells have been also galvanostatically cycled at rate fixed to C/3 for 120 cycles. Figure 5e-f and Figure S6 in the Supplementary material report the related cycling behavior and voltage profiles, respectively. The two cells deliver a maximum specific capacity above 800 mAh g_S^{-1}, which is reflected into areal capacity of about 2.3 mAh cm^{-2}, referred to the geometric surface of the carbon electrode, with slightly higher value for the cell using the DEGDME–Li_2S_8–1m $LiNO_3$–1m $LiCF_3SO_3$ catholyte, likely due to the above mentioned effect of the higher lithium transference number with respect to the cell using the DEGDME–Li_2S_8–1m $LiNO_3$–1m LiTFSI catholyte [28]. The cells exhibit very stable cycling behavior, a Coulombic efficiency above 99.5% after the first cycle (Figure 5e, f), and relatively low polarization [9] (Figure S6). Moreover, the Li/DEGDME–Li_2S_8–1m $LiNO_3$–1m LiTFSI/C cell undergoes the above discussed activation process upon the first 10 cycles, in agreement with the EIS results of Figure 4 [66,67]. Although the observed capacity values may be lower than those reported for Li-S cells using a solid configuration sulfur electrode [9], the semi-liquid configuration benefits from various advantages including easy cell assembling, simple electrode and separator engineering to ensure suitable cycling behavior, and high stability of the electrode/catholyte interphase [14].
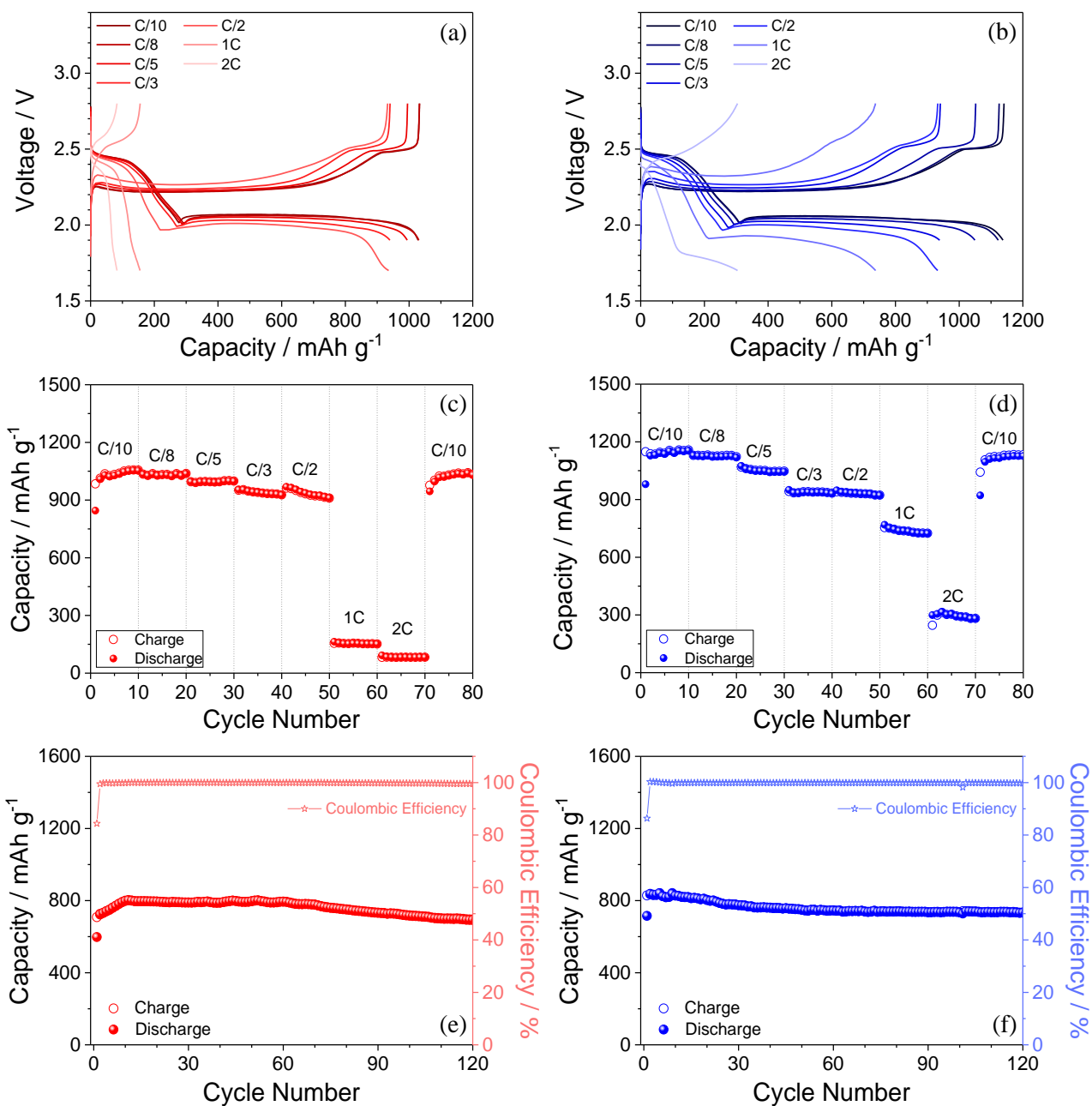
24

Figure 5. (a,b) Galvanostatic voltage profile at C/10, C/8, C/5, C/3, C/2, 1C and 2C rates (1C = 1675 mA g_S^{-1}) of (**a**) Li/DEGDME–Li$_2$S$_8$–1m LiNO$_3$–1m LiTFSI/C and (**b**) Li/DEGDME–Li$_2$S$_8$–1m LiNO$_3$–1m LiCF$_3$SO$_3$/C cells, and (**c,d**) corresponding cycling trends, respectively. Voltage range of 1.9 V – 2.8 V from C/10 to C/3, and of 1.7 V – 2.8 V from C/2 to 2C. (**e,f**) Galvanostatic cycling trend and corresponding Coulombic efficiency (left y-axis) of (**e**) Li/DEGDME–Li$_2$S$_8$–1m LiNO$_3$–1m LiTFSI/C and (**f**) Li/DEGDME–Li$_2$S$_8$–1m LiNO$_3$–1m LiCF$_3$SO$_3$/C cells at C/3 rate (1C = 1675 mA g_S^{-1}) within 1.8 V – 2.8 V range.

25

In order to further highlight the practical interest of the battery herein proposed we attempted to additionally enhance the areal capacity by doubling the catholyte volume to increase the sulfur loading in the cells from 4.4 and 4.2 mg to 8.9 and 8.4 mg for DEGDME–Li_2S_8–1m $LiNO_3$–1m LiTFSI and DEGDME–Li_2S_8–1m $LiNO_3$–1m $LiCF_3SO_3$, respectively. Preliminary cycling, performed at a current rate of C/20 (1C = 1675 mA g_S^{-1}) using 2032-coin cells and shown in Figure S8 of the Supplementary material, reveal areal-capacity approaching 4 mAh cm^{-2} referred to the geometric surface of the carbon electrode, *i.e.*, a value even higher than that of high-performance Li-ion batteries [4], with negligible cell polarization increase. On the other hand, the cells using 4.4 and 4.2 mg for DEGDME–Li_2S_8–1m $LiNO_3$–1m LiTFSI and DEGDME–Li_2S_8–1m $LiNO_3$–1m $LiCF_3SO_3$, respectively, deliver a maximum areal capacity at C/10 rate of about 3 mAh cm^{-2}. Despite the high-loading cells are actually characterized by a higher areal capacity compared to the low-loading ones, they have a smaller practical gravimetric energy density owing to lower sulfur utilization and higher electrolyte content, and require a C-rate low enough to ensure suitable c values. A further possible drawback is the higher electrolyte volume of high-loading cells compared to low-loading ones, which is expected to hinder pouch and winding-type cells assembling. Indeed, the latter configurations are typically characterized by a smaller "dead" volume which may limit the electrolyte content as well as the tolerate contraction/expansion associated with the conversion reaction [13]. Accordingly, further studies aiming to set up the optimal electrolyte amount are certainly required.

Conclusions

Catholyte-type lithium sulfur battery based on a dissolved polysulfide active material was investigated as a viable energy storage system. Li_2S_8 was chemically synthetized in DEGDME solvent and added by either LiTFSI or $LiCF_3SO_3$, as well as by $LiNO_3$ film forming additive, leading to nominal polysulfide concentration of 5 wt.%. X-ray photoelectron spectroscopy revealed the chemical bonds characteristics of the catholyte species, and suggested Li_2S_8 as the main

polysulfide component, along with possible minor amount of Li_2S_6 and Li_2S_4. The solutions were stable up to evaporation, which started at about 70-80 °C, and exhibited a main weight loss at about 157 and 150 °C when LiTFSI and $LiCF_3SO_3$ were used, respectively. The electrochemical characterization, performed through electrochemical impedance spectroscopy, chronoamperometry, voltammetry and galvanostatic cycling, evidenced high conductivity, fast Li^+ transport, suitable lithium passivation properties, wide electrochemical stability window, and low cell polarization. Relevantly, the catholyte using LiTFSI revealed a higher conductivity while lower lithium transference number with respect to the one using the $LiCF_3SO_3$, that is, 3×10^{-3} S cm^{-1} and 0.6 with respect to 2×10^{-3} S cm^{-1} and 0.79 at room temperature, respectively. Reversible Li-S conversion occurred at about 2.4 and 2 V upon reduction, and at about 2.4 V upon oxidation, thereby leading to flat voltage profiles centered at about 2.2 V. Hence, the Li/DEGDME–Li_2S_8–1m $LiNO_3$–1m LiTFSI/C cell delivered a maximum reversible capacity of about 1050 mAh g_S^{-1} at C/10 (1C = 1675 mA g_S^{-1}), while the Li/DEGDME–Li_2S_8–1m $LiNO_3$–1m $LiCF_3SO_3$/C one revealed a capacity approaching 1160 mAh g_S^{-1} at the same current, and a better performance at the elevated currents (1C and 2C), as ascribed the high lithium transference number. Both cells deliver nearly 800 mAh g_S^{-1} with Coulombic efficiency above 99.5% during 120 galvanostatic cycles at C/3 rate, and exhibited a maximum areal capacity of about 4 mAh cm^{-2}. Therefore, the cells can theoretically store maximum energy densities ranging from 2200 to 2440 Wh kg_S^{-1}, respectively, which might be reflected into high practical energy.

Acknowledgements

Supplementary material

Photographs of DEGDME–Li_2S_8–1m $LiNO_3$–1m LiTFSI and DEGDME–Li_2S_8–1m $LiNO_3$–1m $LiCF_3SO_3$ catholytes (Fig. S1). Analyses of O 1*s*, C 1*s*, F 1*s*, N 1*s*, and Li 1*s* XPS signals of DEGDME–Li_2S_8–1m $LiNO_3$–1m LiTFSI (Fig. S2) and DEGDME–Li_2S_8–1m $LiNO_3$–1m $LiCF_3SO_3$ (Fig. S3) catholytes. Percent atomic composition of catholytes using LiTFSI and $LiCF_3SO_3$ salts as determined by XPS (Table S1). Chronoamperometric curves and EIS Nyquist plots before and after cell polarization used for the determination of Li transference number of DEGDME–Li_2S_8–1m $LiNO_3$–1m LiTFSI and DEGDME–1m $LiNO_3$–Li_2S_8–1m $LiCF_3SO_3$ catholytes (Fig. S4). Steady state CV profiles of Li/DEGDME–Li_2S_8–1m $LiNO_3$–1m LiTFSI/C and Li/DEGDME–1m $LiNO_3$–Li_2S_8–1m $LiCF_3SO_3$/C cells within 2.8 V – 2.1 V (Fig. S5). Galvanostatic cycling voltage profile of Li/DEGDME–Li_2S_8–1m $LiNO_3$–1m LiTFSI/C and Li/DEGDME–Li_2S_8–1m $LiNO_3$–1m $LiCF_3SO_3$/C cells at C/3 rate within 1.8 V – 2.8 V (Fig. S6). Nyquist plots of electrochemical impedance spectroscopy (EIS) during cycling tests at C/10, C/8, C/5, C/3, C/2, 1C and 2C rates (1C = 1675 mA g_S^{-1}) of Li/DEGDME–Li_2S_8–1m $LiNO_3$–1m LiTFSI/C and Li/DEGDME–Li_2S_8–1m $LiNO_3$–1m $LiCF_3SO_3$/C cells (Fig. S7). Galvanostatic cycling trend of Li/DEGDME–Li_2S_8–1m $LiNO_3$–1m LiTFSI/C and Li/DEGDME–Li_2S_8–1m $LiNO_3$–1m $LiCF_3SO_3$/C cells with catholyte volume increased from 80 μl to 160 μl, and corresponding steady-state voltage profiles at C/20 rate within 1.8 V – 2.8 V (Fig. S8).

References

[1]   L. Zhou, K. Zhang, Z. Hu, Z. Tao, L. Mai, Y.-M. Kang, S.-L. Chou, J. Chen, Recent developments on and prospects for electrode materials with hierarchical structures for

lithium-ion batteries, Adv. Energy Mater. 8 (2018) 1701415. doi:10.1002/aenm.201701415.

[2]   K.M. Abraham, Prospects and limits of energy storage in batteries, J. Phys. Chem. Lett. 6 (2015) 830–844. doi:10.1021/jz5026273.

[3]   B. Scrosati, History of lithium batteries, J. Solid State Electrochem. 15 (2011) 1623–1630. doi:10.1007/s10008-011-1386-8.

[4]   D. Di Lecce, R. Verrelli, J. Hassoun, Lithium-ion batteries for sustainable energy storage: recent advances towards new cell configurations, Green Chem. 19 (2017) 3442–3467. doi:10.1039/C7GC01328K.

[5]   G.A. Elia, U. Ulissi, S. Jeong, S. Passerini, J. Hassoun, Exceptional long-life performance of lithium-ion batteries using ionic liquid-based electrolytes, Energy Environ. Sci. 9 (2016) 3210–3220. doi:10.1039/C6EE01295G.

[6]   B. Scrosati, K.M. Abraham, W. Van Schalkwijk, J. Hassoun, eds., Lithium batteries, John Wiley & Sons, Inc., Hoboken, NJ, USA, 2013. doi:10.1002/9781118615515.

[7]   R. Fang, S. Zhao, Z. Sun, D.-W. Wang, H.-M. Cheng, F. Li, More Reliable lithium-sulfur batteries: status, solutions and prospects, Adv. Mater. 29 (2017) 1606823. doi:10.1002/adma.201606823.

[8]   M. Hagen, D. Hanselmann, K. Ahlbrecht, R. Maça, D. Gerber, J. Tübke, Lithium-sulfur cells: the gap between the state-of-the-art and the requirements for high energy battery cells, Adv. Energy Mater. 5 (2015) 1401986. doi:10.1002/aenm.201401986.

[9]   L. Carbone, S.G. Greenbaum, J. Hassoun, Lithium sulfur and lithium oxygen batteries: new frontiers of sustainable energy storage, Sustain. Energy Fuels. 1 (2017) 228–247. doi:10.1039/C6SE00124F.

[10]   A. Manthiram, Y. Fu, S. Chung, C. Zu, Y. Su, Rechargeable lithium–sulfur batteries, Chem. Rev. 114 (2014) 11751–11787. doi:10.1021/cr500062v.

[11]   B. Scrosati, J. Hassoun, Y.-K. Sun, Lithium-ion batteries. A look into the future, Energy Environ. Sci. 4 (2011) 3287. doi:10.1039/c1ee01388b.

29

[12] A. Manthiram, S.-H. Chung, C. Zu, Lithium-sulfur batteries: progress and prospects, Adv. Mater. 27 (2015) 1980–2006. doi:10.1002/adma.201405115.

[13] H.-J. Peng, J.-Q. Huang, X.-B. Cheng, Q. Zhang, Review on high-loading and high-energy lithium-sulfur batteries, Adv. Energy Mater. 7 (2017) 1700260. doi:10.1002/aenm.201700260.

[14] Q. Pang, X. Liang, C.Y. Kwok, L.F. Nazar, Advances in lithium–sulfur batteries based on multifunctional cathodes and electrolytes, Nat. Energy. 1 (2016) 16132. doi:10.1038/nenergy.2016.132.

[15] L. Carbone, T. Coneglian, M. Gobet, S. Munoz, M. Devany, S. Greenbaum, J. Hassoun, A simple approach for making a viable, safe, and high-performances lithium-sulfur battery, J. Power Sources. 377 (2018) 26–35. doi:10.1016/j.jpowsour.2017.11.079.

[16] M. Li, W. Wahyudi, P. Kumar, F. Wu, X. Yang, H. Li, L.-J. Li, J. Ming, Scalable approach to construct free-standing and flexible carbon networks for lithium–sulfur battery, ACS Appl. Mater. Interfaces. 9 (2017) 8047–8054. doi:10.1021/acsami.6b12546.

[17] J. Kim, D.J. Lee, H.G. Jung, Y.K. Sun, J. Hassoun, B. Scrosati, An advanced lithium-sulfur battery, Adv. Funct. Mater. 23 (2013) 1076–1080. doi:10.1002/adfm.201200689.

[18] J. Guo, J. Zhang, F. Jiang, S. Zhao, Q. Su, G. Du, Microporous carbon nanosheets derived from corncobs for lithium–sulfur batteries, Electrochim. Acta. 176 (2015) 853–860. doi:10.1016/j.electacta.2015.07.077.

[19] N. Moreno, A. Caballero, J. Morales, M. Agostini, J. Hassoun, Lithium battery using sulfur infiltrated in three-dimensional flower-like hierarchical porous carbon electrode, Mater. Chem. Phys. 180 (2016) 82–88. doi:10.1016/j.matchemphys.2016.05.044.

[20] K. Xi, P.R. Kidambi, R. Chen, C. Gao, X. Peng, C. Ducati, S. Hofmann, R.V. Kumar, Binder free three-dimensional sulphur/few-layer graphene foam cathode with enhanced high-rate capability for rechargeable lithium sulphur batteries, Nanoscale. 6 (2014) 5746–5753. doi:10.1039/C4NR00326H.

[21] M. Agostini, D.-H. Lim, M. Sadd, J.-Y. Hwang, S. Brutti, J.W. Heo, J.H. Ahn, Y.K. Sun, A. Matic, Rational design of low cost and high energy lithium batteries through tailored fluorine-free electrolyte and nanostructured S/C composite, ChemSusChem. (2018). doi:10.1002/cssc.201801017.

[22] X. Liang, A. Garsuch, L.F. Nazar, Sulfur cathodes based on conductive MXene nanosheets for high-performance lithium-sulfur batteries, Angew. Chemie Int. Ed. 54 (2015) 3907–3911. doi:10.1002/anie.201410174.

[23] H.M. Kim, H.-H. Sun, I. Belharouak, A. Manthiram, Y.-K. Sun, An alternative approach to enhance the performance of high sulfur-loading electrodes for Li–S batteries, ACS Energy Lett. 1 (2016) 136–141. doi:10.1021/acsenergylett.6b00104.

[24] M. Li, Y. Wan, J.K. Huang, A.H. Assen, C.E. Hsiung, H. Jiang, Y. Han, M. Eddaoudi, Z. Lai, J. Ming, L.J. Li, Metal-organic framework-based separators for enhancing Li-S battery stability: mechanism of mitigating polysulfide diffusion, ACS Energy Lett. 2 (2017) 2362–2367. doi:10.1021/acsenergylett.7b00692.

[25] J. Ming, M. Li, P. Kumar, L.J. Li, Multilayer approach for advanced hybrid lithium battery, ACS Nano. 10 (2016) 6037–6044. doi:10.1021/acsnano.6b01626.

[26] S. Zhang, K. Ueno, K. Dokko, M. Watanabe, Recent advances in electrolytes for lithium-sulfur batteries, Adv. Energy Mater. 5 (2015) 1500117. doi:10.1002/aenm.201500117.

[27] M. Agostini, J. Hassoun, A lithium-ion sulfur battery using a polymer, polysulfide-added membrane, Sci. Rep. 5 (2015) 7591. doi:10.1038/srep07591.

[28] L. Carbone, M. Gobet, J. Peng, M. Devany, B. Scrosati, S. Greenbaum, J. Hassoun, Comparative study of ether-based electrolytes for application in lithium-sulfur battery, ACS Appl. Mater. Interfaces. 7 (2015) 13859–13865. doi:10.1021/acsami.5b02160.

[29] A. Benítez, D. Di Lecce, Á. Caballero, J. Morales, E. Rodríguez-Castellón, J. Hassoun, Lithium sulfur battery exploiting material design and electrolyte chemistry: 3D graphene framework and diglyme solution, J. Power Sources. 397 (2018).

31

doi:10.1016/j.jpowsour.2018.07.002.

[30] D.-J. Lee, M. Agostini, J.-W. Park, Y.-K. Sun, J. Hassoun, B. Scrosati, Progress in lithium-sulfur batteries: the effective role of a polysulfide-added electrolyte as buffer to prevent cathode dissolution, ChemSusChem. 6 (2013) 2245–2248. doi:10.1002/cssc.201300313.

[31] S.-K. Lee, S.-M. Oh, E. Park, B. Scrosati, J. Hassoun, M.-S.S. Park, Y.-J.J. Kim, H. Kim, I. Belharouak, Y.-K.K. Sun, Highly cyclable lithium–sulfur batteries with a dual-type sulfur cathode and a lithiated Si/SiO_x nanosphere anode, Nano Lett. 15 (2015) 2863–2868. doi:10.1021/nl504460s.

[32] Y. Yang, G. Zheng, Y. Cui, A membrane-free lithium/polysulfide semi-liquid battery for large-scale energy storage, Energy Environ. Sci. 6 (2013) 1552. doi:10.1039/c3ee00072a.

[33] X. Li, X. Pu, S. Han, M. Liu, C. Du, C. Jiang, X. Huang, T. Liu, W. Hu, Enhanced performances of Li/polysulfide batteries with 3D reduced graphene oxide/carbon nanotube hybrid aerogel as the polysulfide host, Nano Energy. 30 (2016) 193–199. doi:10.1016/j.nanoen.2016.10.015.

[34] X. Pu, G. Yang, C. Yu, Liquid-type cathode enabled by 3D sponge-like carbon nanotubes for high energy density and long cycling life of Li-S batteries, Adv. Mater. 26 (2014) 7456–7461. doi:10.1002/adma.201403337.

[35] S. Kim, H. Song, Y. Jeong, Flexible catholyte@carbon nanotube film electrode for high-performance lithium sulfur battery, Carbon N. Y. 113 (2017) 371–378. doi:10.1016/j.carbon.2016.11.019.

[36] R. Demir-Cakan, M. Morcrette, Gangulibabu, A. Guéguen, R. Dedryvère, J.-M. Tarascon, Li–S batteries: simple approaches for superior performance, Energy Environ. Sci. 6 (2013) 176. doi:10.1039/c2ee23411d.

[37] X. Yu, Z. Bi, F. Zhao, A. Manthiram, Hybrid lithium–sulfur batteries with a solid electrolyte membrane and lithium polysulfide catholyte, ACS Appl. Mater. Interfaces. 7 (2015) 16625–16631. doi:10.1021/acsami.5b04209.

[38] H.D. Shin, M. Agostini, I. Belharouak, J. Hassoun, Y.-K. Sun, High-power lithium polysulfide-carbon battery, Carbon N. Y. 96 (2016) 125–130. doi:10.1016/j.carbon.2015.09.034.

[39] S.S. Zhang, J.A. Read, A new direction for the performance improvement of rechargeable lithium/sulfur batteries, J. Power Sources. 200 (2012) 77–82. doi:10.1016/j.jpowsour.2011.10.076.

[40] F.Y. Fan, W.H. Woodford, Z. Li, N. Baram, K.C. Smith, A. Helal, G.H. McKinley, W.C. Carter, Y.-M. Chiang, Polysulfide flow batteries enabled by percolating nanoscale conductor networks, Nano Lett. 14 (2014) 2210–2218. doi:10.1021/nl500740t.

[41] M. Agostini, S. Xiong, A. Matic, J. Hassoun, Polysulfide-containing glyme-based electrolytes for lithium sulfur battery, Chem. Mater. 27 (2015) 4604–4611. doi:10.1021/acs.chemmater.5b00896.

[42] M. Agostini, D.-J. Lee, B. Scrosati, Y.K. Sun, J. Hassoun, Characteristics of Li_2S_8-tetraglyme catholyte in a semi-liquid lithium–sulfur battery, J. Power Sources. 265 (2014) 14–19. doi:10.1016/j.jpowsour.2014.04.074.

[43] J. Evans, C. a. Vincent, P.G. Bruce, Electrochemical measurement of transference numbers in polymer electrolytes, Polymer. 28 (1987) 2324–2328. doi:10.1016/0032-3861(87)90394-6.

[44] M. Agostini, J.-Y. Hwang, H.M. Kim, P. Bruni, S. Brutti, F. Croce, A. Matic, Y.-K. Sun, Minimizing the electrolyte volume in Li-S batteries: a step forward to high gravimetric energy density, Adv. Energy Mater. (2018) 1801560. doi:10.1002/aenm.201801560.

[45] D. Ensling, M. Stjerndahl, A. Nytén, T. Gustafsson, J.O. Thomas, A comparative XPS surface study of Li_2FeSiO_4/C cycled with LiTFSI- and $LiPF_6$ -based electrolytes, J. Mater. Chem. 19 (2009) 82–88. doi:10.1039/B813099J.

[46] G.M. Veith, J. Nanda, L.H. Delmau, N.J. Dudney, Influence of lithium salts on the discharge chemistry of Li–air cells, J. Phys. Chem. Lett. 3 (2012) 1242–1247. doi:10.1021/jz300430s.

[47] J. Mattsson, J.. Forrest, A. Krozer, U. Södervall, A. Wennerberg, L.. Torell, Characterisation

of sub micron salt-doped polymer electrolyte films, Electrochim. Acta. 45 (2000) 1453–1461. doi:10.1016/S0013-4686(99)00359-X.

[48] R. Dedryvère, S. Leroy, H. Martinez, F. Blanchard, D. Lemordant, D. Gonbeau, XPS valence characterization of lithium salts as a tool to study electrode/electrolyte interfaces of Li-ion batteries, J. Phys. Chem. B. 110 (2006) 12986–12992. doi:10.1021/jp061624f.

[49] D. Sharon, D. Hirsberg, M. Afri, F. Chesneau, R. Lavi, A.A. Frimer, Y.-K. Sun, D. Aurbach, Catalytic behavior of lithium nitrate in Li-O_2 cells, ACS Appl. Mater. Interfaces. 7 (2015) 16590–16600. doi:10.1021/acsami.5b04145.

[50] M.U.M. Patel, R. Demir-Cakan, M. Morcrette, J.-M. Tarascon, M. Gaberscek, R. Dominko, Li-S battery analyzed by UV/Vis in operando mode, ChemSusChem. 6 (2013) 1177–1181. doi:10.1002/cssc.201300142.

[51] M.U.M. Patel, R. Dominko, Application of in operando UV/Vis spectroscopy in lithium-sulfur batteries, ChemSusChem. 7 (2014) 2167–2175. doi:10.1002/cssc.201402215.

[52] J. Neubauer, E. Wood, Thru-life impacts of driver aggression, climate, cabin thermal management, and battery thermal management on battery electric vehicle utility, J. Power Sources. 259 (2014) 262–275. doi:10.1016/j.jpowsour.2014.02.083.

[53] D. Di Lecce, C. Fasciani, B. Scrosati, J. Hassoun, A gel–polymer Sn–C/LiMn$_{0.5}$Fe$_{0.5}$PO$_4$ battery using a fluorine-free salt, ACS Appl. Mater. Interfaces. 7 (2015) 21198–21207. doi:10.1021/acsami.5b05179.

[54] D. Shanmukaraj, S. Grugeon, S. Laruelle, M. Armand, Hindered glymes for graphite-compatible electrolytes, ChemSusChem. 8 (2015) 2691–2695. doi:10.1002/cssc.201500502.

[55] M.S. Ding, Electrolytic conductivity and glass transition temperature as functions of salt content, solvent composition, or temperature for LiPF$_6$ in propylene carbonate + diethyl carbonate, J. Chem. Eng. Data. 48 (2003) 519–528. doi:10.1021/je020219o.

[56] A. Jarosik, S.R. Krajewski, A. Lewandowski, P. Radzimski, Conductivity of ionic liquids in mixtures, J. Mol. Liq. 123 (2006) 43–50. doi:10.1016/j.molliq.2005.06.001.

[57] C. Zu, A. Manthiram, Stabilized lithium–metal surface in a polysulfide-rich environment of lithium–sulfur batteries, J. Phys. Chem. Lett. 5 (2014) 2522–2527. doi:10.1021/jz501352e.

[58] M. Agostini, B. Scrosati, J. Hassoun, An advanced lithium-ion sulfur battery for high energy storage, Adv. Energy Mater. 5 (2015) 1500481. doi:10.1002/aenm.201500481.

[59] S. Xiong, K. Xie, Y. Diao, X. Hong, On the role of polysulfides for a stable solid electrolyte interphase on the lithium anode cycled in lithium–sulfur batteries, J. Power Sources. 236 (2013) 181–187. doi:10.1016/j.jpowsour.2013.02.072.

[60] S. Phadke, E. Coadou, M. Anouti, Catholyte formulations for high-energy Li–S batteries, J. Phys. Chem. Lett. 8 (2017) 5907–5914. doi:10.1021/acs.jpclett.7b02936.

[61] S. Xiong, K. Xie, Y. Diao, X. Hong, Characterization of the solid electrolyte interphase on lithium anode for preventing the shuttle mechanism in lithium–sulfur batteries, J. Power Sources. 246 (2014) 840–845. doi:10.1016/j.jpowsour.2013.08.041.

[62] D.R. Franceschetti, Interpretation of finite-length-warburg-type impedances in supported and unsupported electrochemical cells with kinetically reversible electrodes, J. Electrochem. Soc. 138 (1991) 1368. doi:10.1149/1.2085788.

[63] L. Carbone, D. Di Lecce, M. Gobet, S. Munoz, M. Devany, S. Greenbaum, J. Hassoun, Relevant features of a triethylene glycol dimethyl ether-based electrolyte for application in lithium battery, ACS Appl. Mater. Interfaces. 9 (2017) 17085–17095. doi:10.1021/acsami.7b03235.

[64] S. Drvarič Talian, J. Moškon, R. Dominko, M. Gaberšček, Reactivity and diffusivity of Li polysulfides: a fundamental study using impedance spectroscopy, ACS Appl. Mater. Interfaces. 9 (2017) 29760–29770. doi:10.1021/acsami.7b08317.

[65] C. Barchasz, F. Molton, C. Duboc, J.-C. Leprêtre, S. Patoux, F. Alloin, Lithium/sulfur cell discharge mechanism: an original approach for intermediate species identification, Anal. Chem. 84 (2012) 3973–3980. doi:10.1021/ac2032244.

[66] L. Carbone, J. Peng, M. Agostini, M. Gobet, M. Devany, B. Scrosati, S. Greenbaum, J.

35

Hassoun, Carbon composites for a high-energy lithium-sulfur battey with a glyme-based electrolyte, ChemElectroChem. 4 (2017) 209–215. doi:10.1002/celc.201600586.

[67] A. Benítez, D. Di Lecce, G.A. Elia, Á. Caballero, J. Morales, J. Hassoun, A lithium-ion battery using a 3 D-array Nanostructured Graphene–Sulfur Cathode and a Silicon Oxide-Based Anode, ChemSusChem. 11 (2018) 1512–1520. doi:10.1002/cssc.201800242.

[68] S.-Y. Lang, R.-J. Xiao, L. Gu, Y.-G. Guo, R. Wen, L.-J. Wan, Interfacial mechanism in lithium–sulfur batteries: how salts mediate the structure evolution and dynamics, J. Am. Chem. Soc. 140 (2018) 8147–8155. doi:10.1021/jacs.8b02057.

[69] R. Cao, J. Chen, K.S. Han, W. Xu, D. Mei, P. Bhattacharya, M.H. Engelhard, K.T. Mueller, J. Liu, J.-G. Zhang, Effect of the anion activity on the stability of Li metal anodes in lithium-sulfur batteries, Adv. Funct. Mater. 26 (2016) 3059–3066. doi:10.1002/adfm.201505074.

[70] R. Dominko, A. Vizintin, G. Aquilanti, L. Stievano, M.J. Helen, A.R. Munnangi, M. Fichtner, I. Arcon, Polysulfides formation in different electrolytes from the perspective of X-ray absorption spectroscopy, J. Electrochem. Soc. 165 (2018) A5014–A5019. doi:10.1149/2.0151801jes.

[71] S.S. Zhang, Effect of discharge cutoff voltage on reversibility of lithium/sulfur batteries with LiNO$_3$-contained electrolyte, J. Electrochem. Soc. 159 (2012) A920–A923. doi:10.1149/2.002207jes.
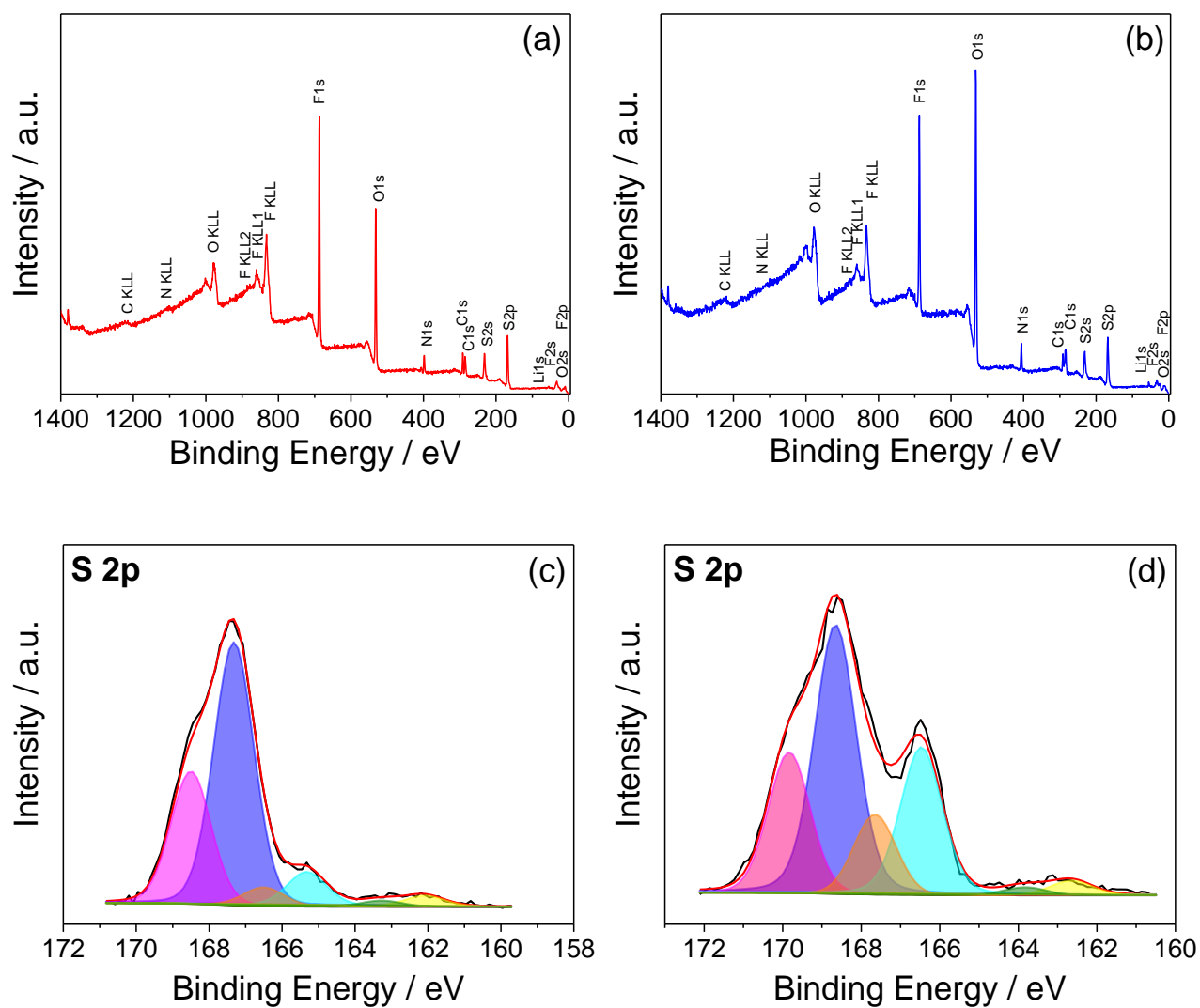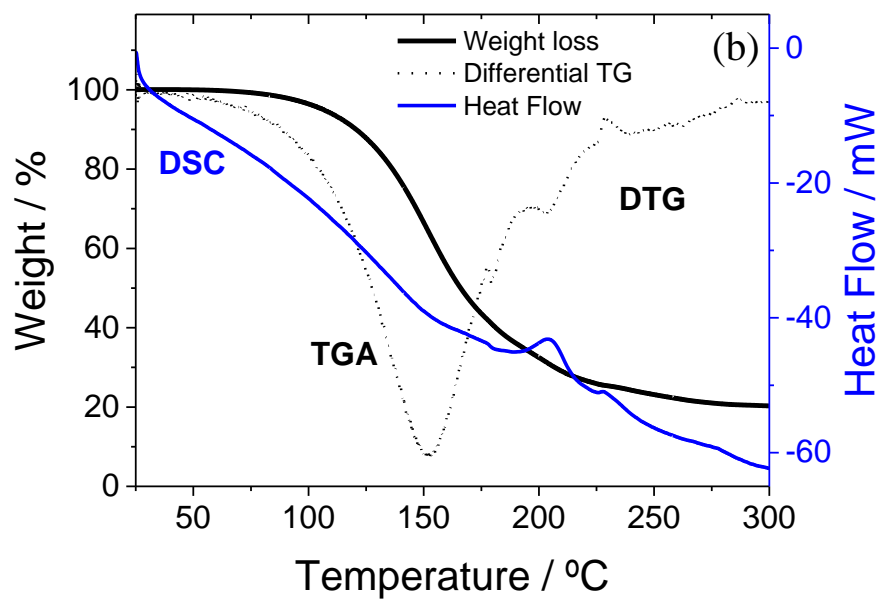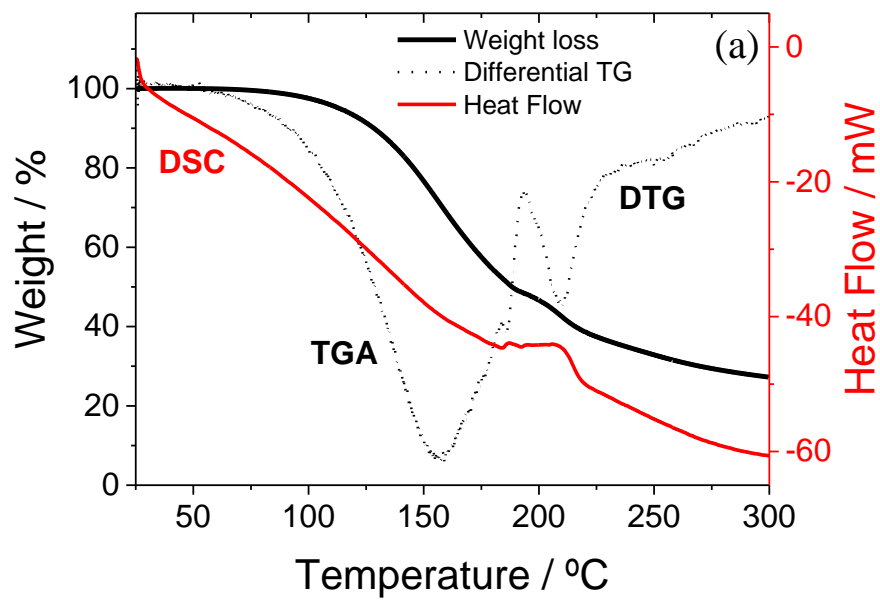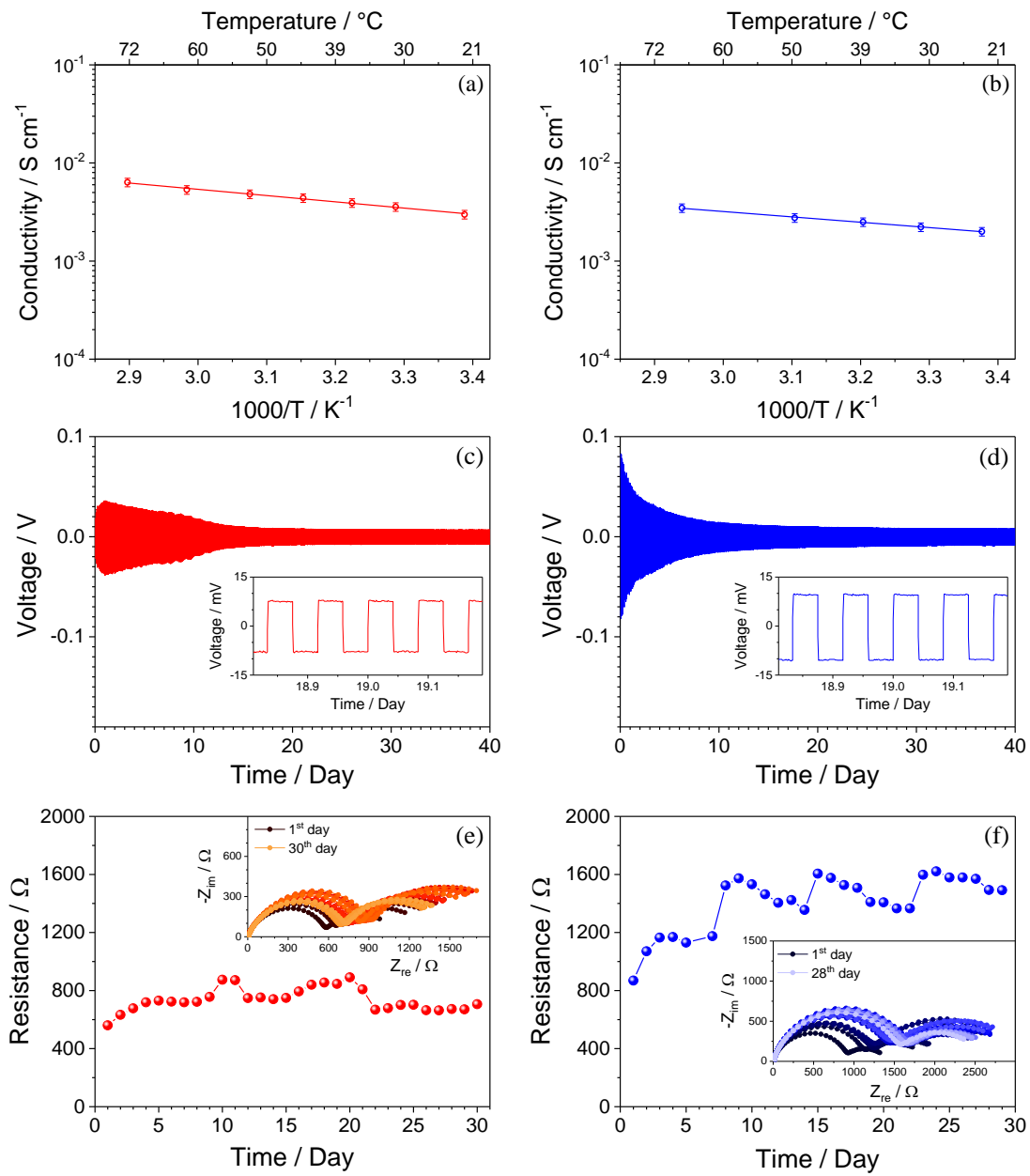
Figure 1

Figure 2

Figure 3

Figure 4
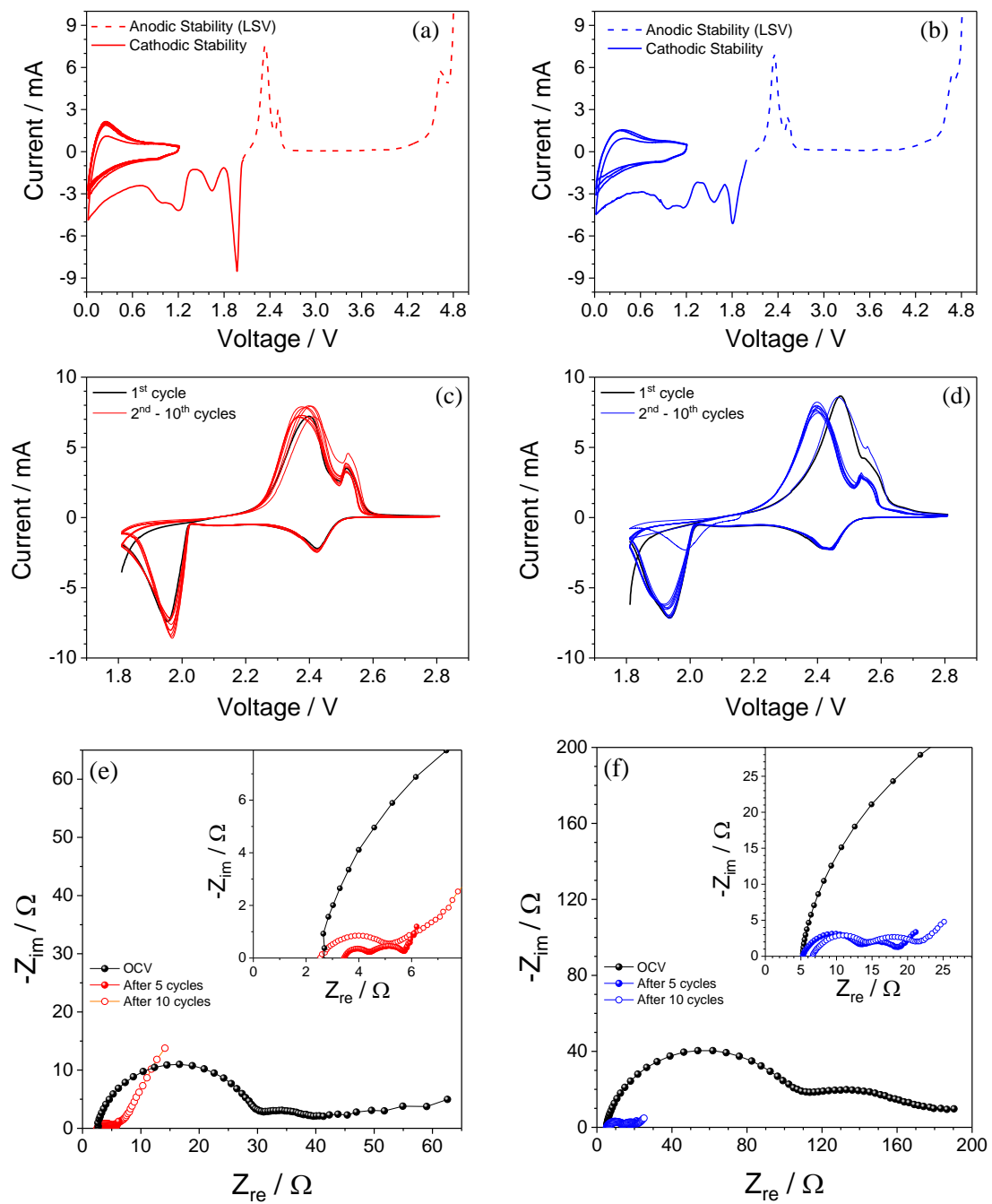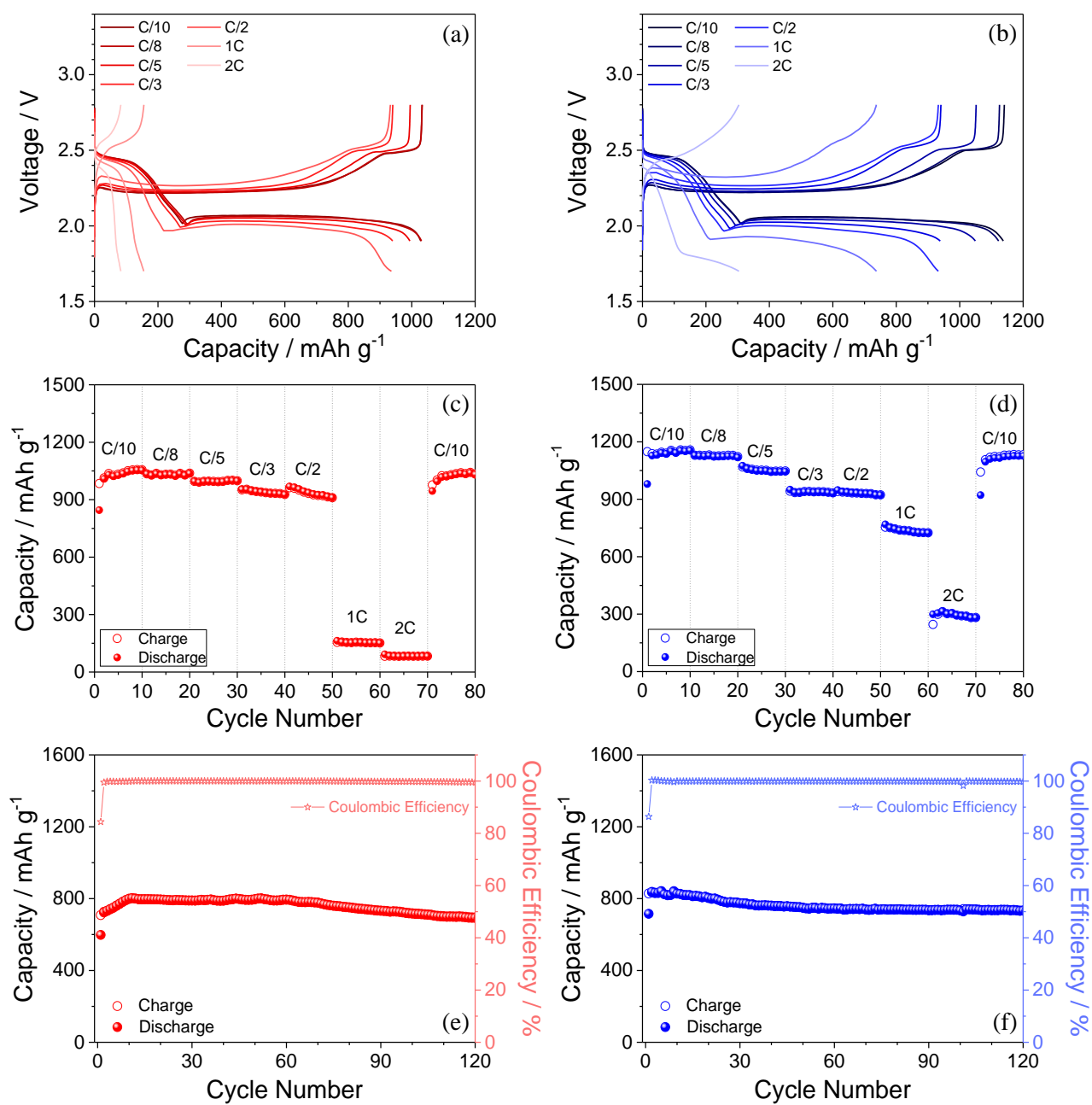
Figure 5

Figure captions

Figure 1. X-ray photoelectron spectra of (**a,c**) DEGDME–Li_2S_8–1m $LiNO_3$–1m LiTFSI and (**b,d**) DEGDME–Li_2S_8–1m $LiNO_3$–1m $LiCF_3SO_3$ catholytes. (**a,b**) Survey spectra and (**c,d**) deconvoluted S 2p core level spectra.

Figure 2. Termogravimetric analysis (TGA), corresponding differential curve (DTG), and differential scanning calorimetry (DSC) curves of (**a**) DEGDME–Li_2S_8–1m $LiNO_3$–1m LiTFSI and (**b**) DEGDME–Li_2S_8–1m $LiNO_3$–1m $LiCF_3SO_3$ samples.

Figure 3. (**a,b**) Ionic conductivity versus temperature of (**a**) DEGDME–Li_2S_8–1m $LiNO_3$–1m LiTFSI and (**b**) DEGDME–Li_2S_8–1m $LiNO_3$–1m $LiCF_3SO_3$ catholytes. (**c,d**) Lithium stripping-deposition galvanostatic test performed at 0.1 mA cm^{-2} and 1 hour step-time of (**c**) DEGDME–Li_2S_8–1m $LiNO_3$–1m LiTFSI and (**d**) DEGDME–Li_2S_8–1m $LiNO_3$–1m $LiCF_3SO_3$ catholytes, with magnifications in panel insets showing steady-state cycles. (**e,f**) Time evolution of the lithium/interface resistance of symmetrical Li/Li cells using (**e**) DEGDME–Li_2S_8–1m $LiNO_3$–1m LiTFSI and (**f**) DEGDME–Li_2S_8–1m $LiNO_3$–1m $LiCF_3SO_3$ catholytes, and corresponding electrochemical impedance spectroscopy (EIS) Nyquist plots in panel insets. Frequency range: 100 kHz – 100 mHz. Signal amplitude: 10 mV.

Figure 4. (**a,b**) Cyclic voltammetry (CV) profiles during cathodic scans and linear sweep voltammetry (LSV) profiles during anodic scan of lithium cells using carbon working electrode (indicated by C in the cell's schemes) with (**a**) DEGDME–Li_2S_8–1m $LiNO_3$–1m LiTFSI and (**b**) DEGDME–Li_2S_8–1m $LiNO_3$–1m $LiCF_3SO_3$ catholytes. (**c,d**) Cyclic voltammetry (CV) profiles of (**c**) Li/DEGDME–Li_2S_8–1m $LiNO_3$–1m LiTFSI/C and (**d**) Li/DEGDME–Li_2S_8–1m $LiNO_3$–1m $LiCF_3SO_3$/C cells within 2.8 V and 1.8 V range. (**e,f**) Nyquist plots of the electrochemical impedance spectroscopy (EIS) during CV tests of (**e**) Li/DEGDME–Li_2S_8–1m $LiNO_3$–1m LiTFSI/C and (**f**) Li/DEGDME–Li_2S_8–1m $LiNO_3$–1m $LiCF_3SO_3$/C cells within 1.8 V and 2.8 V range at the

OCV, after 5 and 10 cycles with magnification in insets. Scan rate: 0.1 mV s^{-1}. Frequency range: 100 kHz – 100 mHz. Signal amplitude: 10 mV.

Figure 5. (a,b) Galvanostatic voltage profile at C/10, C/8, C/5, C/3, C/2, 1C and 2C rates (1C = 1675 mA g$_S^{-1}$) of (**a**) Li/DEGDME–Li$_2$S$_8$–1m LiNO$_3$–1m LiTFSI/C and (**b**) Li/DEGDME–Li$_2$S$_8$–1m LiNO$_3$–1m LiCF$_3$SO$_3$/C cells, and (**c,d**) corresponding cycling trends, respectively. Voltage range of 1.9 V – 2.8 V from C/10 to C/3, and of 1.7 V – 2.8 V from C/2 to 2C. (**e,f**) Galvanostatic cycling trend and corresponding Coulombic efficiency (left y-axis) of (**e**) Li/DEGDME–Li$_2$S$_8$–1m LiNO$_3$–1m LiTFSI/C and (**f**) Li/DEGDME–Li$_2$S$_8$–1m LiNO$_3$–1m LiCF$_3$SO$_3$/C cells at C/3 rate (1C = 1675 mA g$_S^{-1}$) within 1.8 V – 2.8 V range.

Revised Supplementary Materials
Click here to download Supplementary Materials: Revised supplementary material.pdf